# TIDE ADJUSTED WETLAND INDEX (TAWI) FOR GEORGIA SALT MARSH ECOSYSTEMS: A MODEL TO MINIMIZE THE TIDE EFFECT ON MODIS SURFACE REFLECTANCE

by

LI WANG

(Under the Direction of Deepak Mishra)

## ABSTRACT

Tidal effect is one of the primary factors that causes unwarranted variability in salt marsh reflectance characteristics and introduces errors in remote sensing based biophysical models. Tide induced variability is particularly worse in coarse resolution datasets such as Moderate-resolution Imaging Spectroradiometer (MODIS) 250m data where it is not possible to visually detect the affected pixels or scenes. This study presents a novel index, TAWI (Tide Adjusted Wetland Index) for identifying images with no tide or very low tide using temporally dense MODIS data. Logistics regression based TAWI was used to filter out flooded images from MODIS sensor. Overall phenology derived for 15 years pre- and post-TAWI showed that post-TAWI phenology was able to eliminate the noise due to tide influence. Eliminating flooded data from salt marsh phenology using TAWI will provide accurate remote estimation for numerous biophysical parameters including chlorophyll content, above and below ground biomass, and gross primary productivity.

INDEX WORDS: TAWI; Salt marsh; Tide effect; Logistic regression model; MODIS surface reflectance; NDVI; WDRVI; Phenology; PhenoCam

# TIDE ADJUSTED WETLAND INDEX (TAWI) FOR GEORGIA SALT MARSH ECOSYSTEMS: A MODEL TO MINIMIZE THE TIDE EFFECT ON MODIS SURFACE REFLECTANCE

by

LI WANG

B.S., Beijing Normal University, China, 2013

A Thesis Submitted to the Graduate Faculty of The University of Georgia in Partial Fulfillment of the Requirements for the Degree

MASTER OF SCIENCE

ATHENS, GEORGIA

2015

# TIDE ADJUSTED WETLAND INDEX (TAWI) FOR GEORGIA SALT MARSH ECOSYSTEMS: A MODEL TO MINIMIZE THE TIDE EFFECT ON MODIS SURFACE REFLECTANCE

by

LI WANG

| | |
|---|---|
| Major Professor: | Deepak Mishra |
| Committee: | Xiaobai Yao |
| | Marguerite Madden |

Electronic Version Approved:

Suzanne Barbour
Dean of the Graduate School
The University of Georgia
August 2015

ACKNOWLEDGEMENTS

Foremost, I would like to express my sincere appreciation to my advisor Dr. Deepak Mishra for the continuous support of my thesis study and research, for his patience, motivation, enthusiasm, and immense knowledge. His guidance helped me in all the time of research and writing of this thesis. I could not have imagined having a better advisor and mentor for my master study.

Besides my advisor, I would like to thank the rest of my thesis committee: Dr. Marguerite Madden and Dr. Xiaobai Yao, for their encouragement, insightful comments, and hard questions.

My sincere thanks also goes to Dr. Jessica O'Connell. She gave me many constructive recommendations on both research and writing. Literally, she helped me figure out many problems that confused me.

TABLE OF CONTENTS

Page

LIST OF TABLES

Page

LIST OF FIGURES

Page

# CHAPTER 1

# INTRODUCTION

Salt marshes are coastal wetlands that are flooded and drained by tidally delivered salt water (Mitsch & Gosselink, 2007). These marshes are one of the most ecologically and economically productive ecosystems of the world (Alongi, 1998; Eisma et al., 1998). For example, salt marshes have high carbon sequestration potential and carbon flux in salt marshes has a huge influence on the global carbon budget (Gallagher et al., 1980; Smith, et al., 1983; Odum, et al., 1984; Odum, 1998; Connor et al., 2001; Chmura et al., 2003). However, these critical habitats are severely threatened by natural and human activities, such as soil erosion, land use change, hurricanes and oil spills (Gilfillan et al., 1995; White & Morton, 1997; Bryant & Chabreck, 1998; Hester & Mendelssohn, 2000; Sugumaran et al., 2004; Silliman et al., 2009; Mishra et al., 2012). Extensive loss of salt marshes has occurred in many countries throughout the world (Swenson & Turner, 1987; Hackney & Yelverton, 1990; Harbor, 2007; Ravens et al., 2009). Therefore, to prevent further loss of salt marshes and conserve existing salt marsh ecosystems, it is important to manage and monitor salt marsh ecosystems (Ozesmi & Bauer, 2002; Rebelo et al., 2009). Monitoring efforts based only on traditional field sampling are often costly, time consuming, and inadequate to provide a broad regional trend of salt marsh status. Instead, remote sensing has long been used as the preferred tool for conducting salt marsh assessment at multiple scales (Jensen & Lulla, 1987; Adam et al., 2010; Mishra & Ghosh., 2015). While a great number of efforts for monitoring salt marshes using remote sensing have been made, these have largely focused on delineating salt marsh spatial extent and classifying

plant communities (Gross & Klemas, 1986; Malthus & George, 1997; Artigas & Pechmann, 2010; Collin et al., 2010; Davaranche et al., 2010). Few studies have explored remote sensing approaches for estimating biophysical properties of salt marshes, such as Gross Primary Productivity (GPP) (Hardisky et al., 1984; Mishra & Ghosh, 2013). In addition, models estimating biophysical properties that are based on vegetation indices are influenced by tidal variation in salt marshes (Barr et al., 2013). In this thesis, a method will be developed that minimizes tidal effects on remote sensing-based estimates biophysical properties.

For salt marsh monitoring, there are obvious advantages in using remote sensing technology. For example, remote sensing provides a near real-time and cost-effective method for continuous large-area data coverage (Butera, 1983). Historically, aerial photography was the first remote sensing method to be used for exploring salt marshes (Seher & Tueller, 1973; Shima et al., 1976; Howland, 1980). However, it is not practical for continuously monitoring salt marsh ecosystems because it is costly and time-consuming to acquire and process (Adam et al., 2010). With the advent of modern sensors, it is more common to map and monitor salt marshes using satellite remote sensing images. Satellite remote sensors provide cost-efficient alternatives to intensive field surveys in monitoring and assessing coastal ecosystems and their dynamics at appropriate scales and resolutions (Mishra & Ghosh, 2015). Further, selecting an appropriate sensor for field studies requires an evaluation of sensor trade-offs. While, patchiness and fine scale of heterogeneity in salt marshes requires satellite data with high spatial resolution to map boundaries accurately, processes with high temporal variability such as tidal inundation, require high satellite return frequency. Thus, Landsat Thematic Mapper (TM) data, with spatial resolutions of 30 m and 16 d return frequency, are commonly used for salt marsh land cover mapping (Rundquist et al., 2001; Klemas, 2011). The overall goal of this thesis study is to

identify high quality salt marsh data with no tide or very low tide. Tidal inundation has high temporal variability and hence this study requires satellite images have high temporal resolution. NASA's Moderate-resolution Imaging Spectroradiometer (MODIS) is appropriate for this study because of its high temporal resolution of 1 day. 250m and 500m MODIS data have recently been used to analyze the spatio-temporal trend of salt marsh biophysical characteristics such as canopy chlorophyll content, leaf area index, above- and below ground biomass, and gross primary productivity at a regional scale (Mishra & Ghosh, 2015). Tidal effect is one of the primary factors that causes unwarranted variability in salt marsh reflectance characteristics and introduces errors in remote sensing based biophysical models. Tide induced variability is particularly worse in coarse resolution datasets such as MODIS 250m data where it is not possible to visually detect the affected pixels or scenes. Studies dealing with flagging satellite data, in this case MODIS data, is non-existent.

Remote sensing of salt marsh biophysical characteristics is challenging compared to terrestrial vegetation, such as boreal forest, peatlands, grasslands and crops because of water interference (Lorenzen & Jensen, 1988; Adam et al., 2010; Mishra & Ghosh, 2013). Water and moist soil attenuate the intensity of the near-infrared (NIR) in salt marsh, which increases the uncertainty in remote sensing based vegetation indices used for mapping salt marsh health and productivity. The water effect on the salt marsh vegetation is illustrated by two figures (Fig. 1 and Fig. 2). As shown in Fig. 1, salt marshes are located in the western and eastern area of Sapelo Island, Georgia, USA while forests are located in the middle area of this island. The color of salt marsh vegetation in August (growing season) is supposed to be green in the true color image (R, G, B) and red in the false color image (NIR, R, G). However, salt marshes appeared purple rather than green in the true color image (Fig. 1a) and cyan instead of red in the false

color image (Fig. 1b) due to the attenuation of red and NIR reflectance by water respectively. Attenuation of near-infrared signals also makes common vegetation indices such as normalized difference vegetation index (NDVI) and wide dynamic range vegetation index (WDRVI) fluctuate highly for the salt marsh vegetation. NDVI is widely used for monitoring, analyzing, and mapping temporal and spatial distributions of vegetation (DeFries & Townshend, 1994). However, the near-infrared signal of salt marsh vegetation is very weak and hence NDVI preforms poorly across salt marshes. Instead, WDRVI, a vegetation index that enhances the dynamic range of the NDVI by applying a weighting parameter α to near-infrared reflectance, is used in salt marsh vegetation (Gitelson, 2004, Mishra & Ghosh, 2015). In past research, WDRVI α assigned to 0.1 resulted in the most obvious phenology patterns and monitored salt marsh vegetation with the greatest accuracy (Mishra & Ghosh, 2015). Therefore 0.1 was applied as the α level in this thesis study. Fig. 2 depicts the values of NIR reflectance, NDVI and WDRVI for a East-West profile of vegetation types across Sapelo Island. Values of NIR reflectance, NDVI and WDRVI all are much lower in salt marshes than forests because of attenuation of near-infrared signal by water (Fig. 2). Consequently, magnitude of traditional vegetation indices (NDVI and WDRVI) is diminished and can be misleading when used to monitor salt marsh health. Therefore, it is important to develop a method to remove flooded vegetation before using vegetation indices (NDVI and WDRVI) to monitor salt marsh biophysical characteristics.

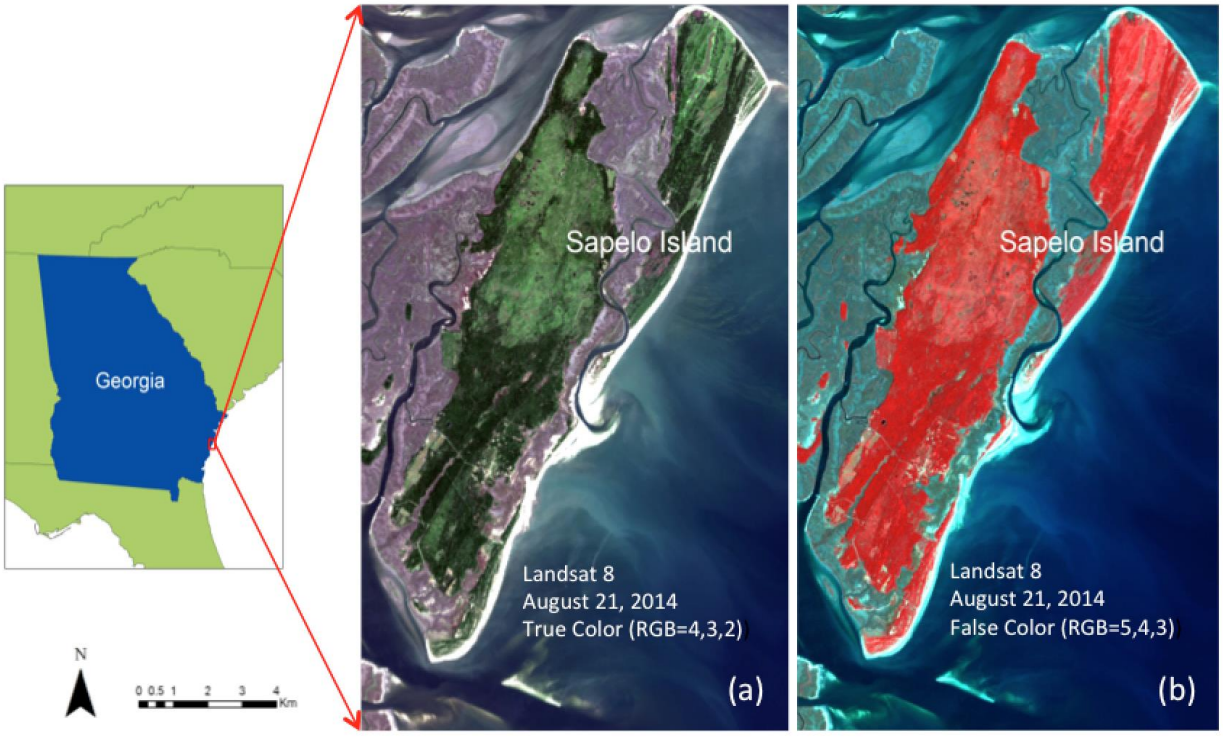


Figure 1. Landsat 8 true color image (a) and false color (b) image of Sapelo Island, a barrier island located in coastal Georgia, USA.

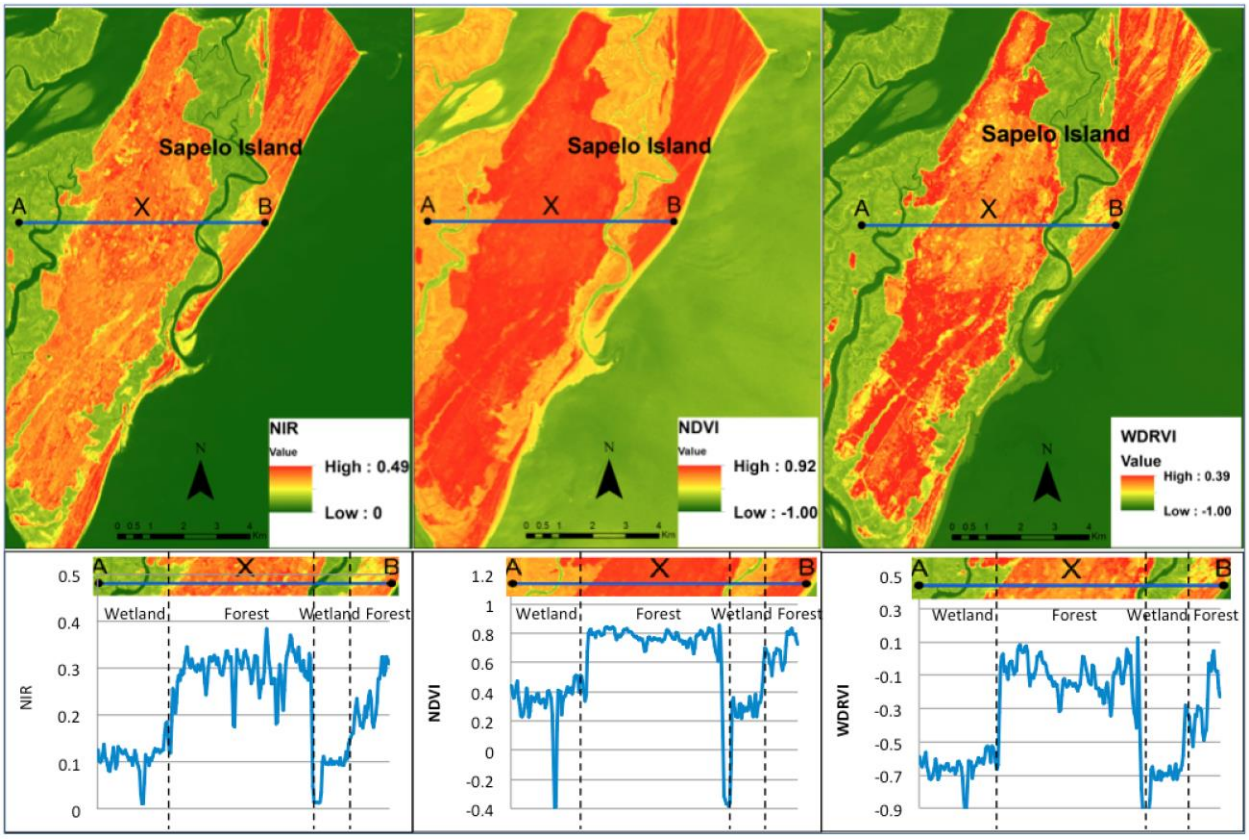


Figure 2. Spatial patterns of NIR surface reflectance (a), NDVI (b), and WDRVI (c) across Sapelo Island, Georgia, USA. There is a transect line X in each of these three maps. The plot graphs under the maps are patterns of NIR reflectance (a), NDVI (b), and WDRVI (c) across a west to east gradient of the transect X.

The purpose of this study is to present a novel approach to obtain MODIS data of identifying high quality salt marshes (no tide or very low tide), that are most suitable for estimating biophysical measures for coastal salt marshes. An index for salt marshes, the tide adjusted wetland index (TAWI), was developed to achieve this goal. TAWI can be used to filter out flooded vegetation from MODIS daily products to avoid daily variability within salt marsh biophysical parameters that results from tidal fluctuations. My specific objectives are: 1) to flag flooded and non-flooded vegetation within the MODIS dataset, 2) to develop a statistical model of classifying these MODIS images as flooded and non-flooded vegetation, 3) to develop a novel

index, TAWI, to identify non-flooded vegetation based on the classification model, and finally 4) to apply the new index across a broad timespan (2000-2015) of MODIS cloud-free images and different salt marsh sites. In the future, this thesis will contribute to the development of novel approaches for estimating biophysical properties such as gross primary productivity of salt marshes using remote sensing techniques.

# CHAPTER 2

# METHODS

## 2.1 Study area

### 2.1.1 Study site description

The study site is located on the western side of the Sapelo Island, GA, USA (Fig. 3), in an area extensively characterized by the Georgia Coastal Ecosystems Long Term Ecological Research (GCE-LTER) program and occupied by the Sapelo Island National Estuarine Research Reserve. Sapelo Island is a barrier island located off the central Georgia coast of the southeastern United States. Sapelo Island is bounded on the east by the Atlantic Ocean and on the west by estuarine waters that comprise the Dolby and Altamaha Sounds and the Duplin River. Sapelo Island is made up of a total of 16,500 acres, of which, nearly 5,600 acres are tidal salt marsh (http://www.sapelonerr.org). Additionally, salt marshes within the study area experience semidiurnal lunar tides with large amplitudes (as much as 3 m) (Więski & Pennings, 2013).

There is an *in-situ* eddy covariance (EC) tower (31° 26' 38.2" N, 81° 17' 1.0" W) within the study area, established by GCE-LTER program. The EC tower measures carbon dioxide, water and energy fluxes between the biosphere and the atmosphere. Currently more than 250 eddy covariance sites are active around the world (Papale et al., 2006). Around the tower the dominant vegetation is short, medium and tall form *Spartina alterniflora*. There also are very small amounts of *Juncus* in the study area. *S. alterniflora* is a perennial deciduous salt tolerant salt marsh graminoid and maximum height averages 1-1.5 m tall. It has smooth and hollow

stems, which bear leaves up to 20-60 cm long and 1.5 cm wide at their base, and which are sharply tapered and bend down at their tips (Duncan & Duncan, 1987).

Attached to the EC tower, there also is a PhenoCam, a digital camera that collects near surface remote-sensing imagery at half-hour time steps. The PhenoCam on Sapelo Island is part of a national network that is used to track vegetation phenology, in terms of seasonal changes in the greenness of the canopy (Richardson, el al., 2011). This is done by recording time-lapse images of a fixed scene over time and then using simple image analysis techniques to extract quantitative color information, red green and blue (RGB) values, from each image. Images from cameras are uploaded to the PhenoCam server every half an hour and thus they provides a near real-time data library of canopy phenology as well as ancillary data. In addition, this approach can be done at relatively low cost, with minimal personnel expense and without the need of human observers (Richardson et al., 2007).

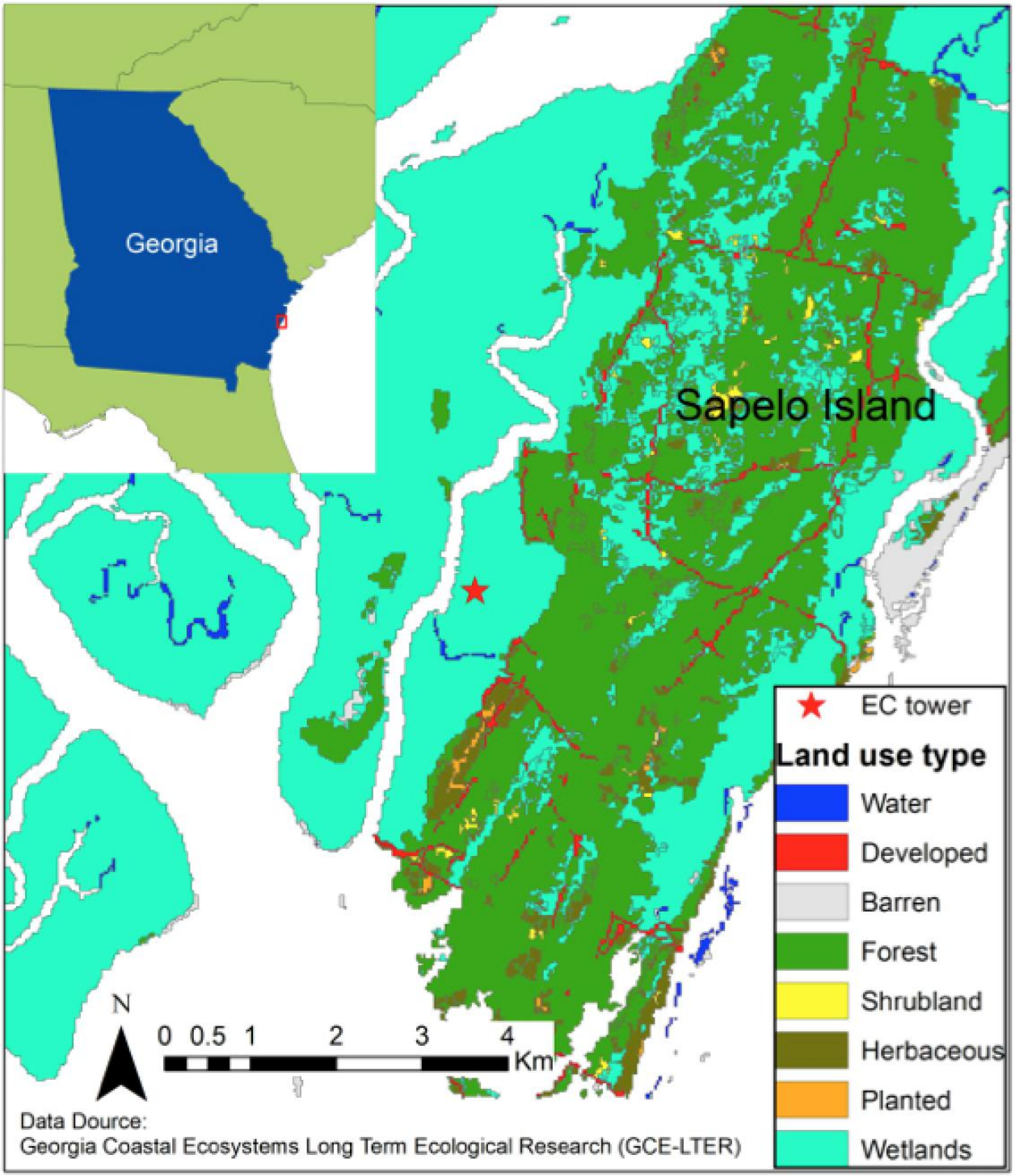


Figure 3. Map of Sapelo Island, GA, USA. The red star represents the study site where the EC tower locates. The base map shows the land cover types on Sapelo Island, Georgia, USA. The insert in the top left is the overview map of the study area.

### 2.1.2 Selecting MODIS study pixels

As a first step in developing the TAWI, the vegetated marshes at the study site were necessary to be identified whether they were tidally inundated. The tidally classified images from the PhenoCam were used for this effort. The PhenoCam at the GCE-LTER has collected data from 2013-09-16 to the present (Fig. 4). The PhenoCam images for this thesis study were collected from 2013-09-16 to 2015-05-31. However, because of mechanical failure, PhenoCam data are lacking between 2014-07-16 and 2014-09-01. The PhenoCam images were used because of 1) easy accessibility to the PhenoCam library and 2) the high temporal resolution (every half-hour) of PhenoCam data, providing relatively accurate information of tidal status.


Figure 4. PhenoCam image captured at 11:30am on September 19th, 2013.

To select focal MODIS pixels for this study, pixels selected were ensured to cover an area of marsh that was both near to the Phenocam and sampled the majority of the marsh within the PhenoCam field-of-view. As shown in Fig. 5, the nearest MODIS pixel (MODIS pixel 1) contains the EC tower. Additionally, there is a creek in the top of the PhenoCam image (also presented in the Google Earth map, see Fig. 5). The area beyond the creek is too oblique in the PhenoCam view to extract useful data. Therefore, MODIS pixel 2 provided the best coverage of marshes between the creek and the EC tower. As a result, MODIS pixels 1 and 2 were selected to be focal study pixels.


Figure 5. PhenoCam field of view and corresponding MODIS pixel footprints. The base map shows the Google Earth map of the study area. The red star is the location of the EC tower. The yellow polygons are six pixel footprints of MOD09GQ product. The red polygon region presents

the PhenoCam field of view. The blue line is a creek within the study area. The insert in the top left is the PhenoCam image showing the position of creek.

## 2.2 Flagging flood status for MODIS pixels

### 2.2.1 Filtering MODIS daily data to cloud-free images

MODIS daily data was necessary to be filtered to cloud-free images in order to retain MODIS images best suited for tide effect analysis. The research pixels are located within the MODIS grid h11v05 (Fig. 6). Two MODIS products, MOD09GQ and MOD09GA, were used to identify cloud-free images. MOD09GQ is a surface reflectance product, which provides two channels of reflectance data at a 250m resolution in a daily gridded L2G product in the Sinusoidal projection. Within MOD09GQ, Band 1 corresponds to the red spectrum (620-670 nm) (hereafter the MODIS "red band") and Band 2 corresponds to the near-infrared spectrum (841-876 nm) (hereafter the MODIS "NIR band") (Vermote et al., 2011). Another MODIS product, MOD09GA, provides information on cloudiness over a 1-km spatial resolution in a daily gridded L2G product in the Sinusoidal projection. It also provides important pixel quality and viewing geometry information for MODIS products, including an accurate cloud mask that can be used in conjunction with MOD09GQ products to flag cloudy pixels (Vermote et al., 2011).

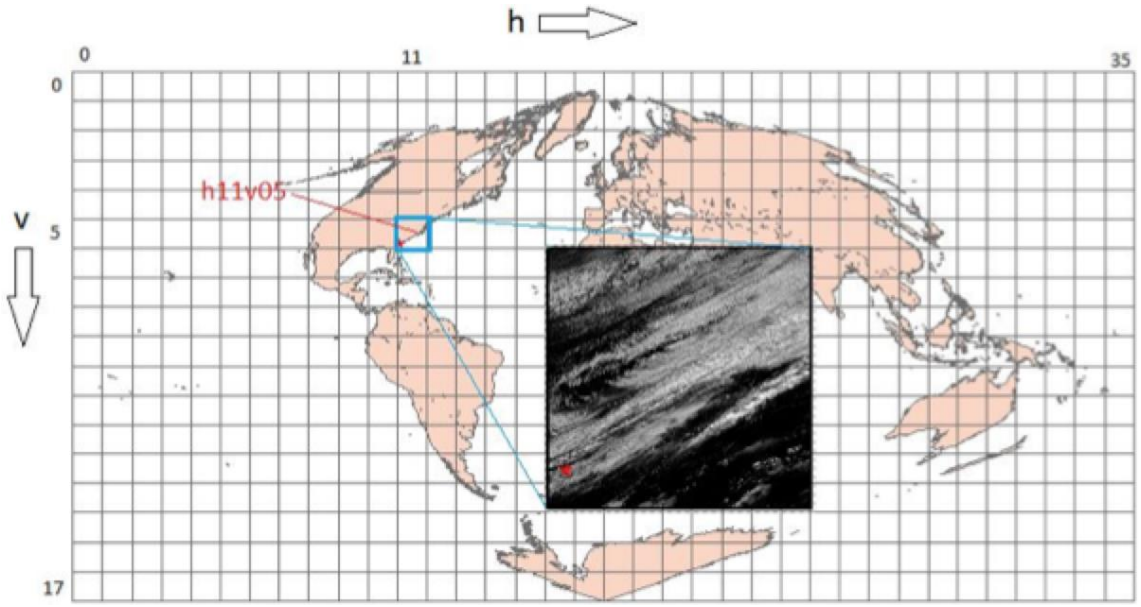


Figure 6. MODIS grids map of the world. The study site (red star) is shown in the inset and is located in grid h11v05.

The surface reflectance values of red and NIR bands of two focal study pixels were obtained from MOD09GQ dataset (hereafter the "spectral reflectance dataset"). Reflectance information for the red and NIR bands was stored in two different layers of spectral reflectance dataset. First, these two layers were extracted separately using their indexes via Python scripts and the original reflectance values of the study pixels were acquired based on their locations. Then, the real reflectance values were calculated by multiplying the original reflectance values by 0.0001 since they were stored by a scale factor of 0.0001 in the dataset. And finally, the average real reflectance value of two study pixels was applied as the reflectance value of study area for that sample date. As a result, the average red and NIR reflectance data of the study area was obtained for each day from 2000-02-24 to 2015-05-31. Since there was no MODIS surface reflectance products before 2000-02-24, the data collection period was from 2000-02-24 to 2015-05-31.

Further, the cloud state information that was recorded in the "*State_1km: Reflectance Data State"* layer (hereafter the "cloud state layer") within the MOD09GA dataset was used to filter out cloudy pixels from spectral reflectance dataset. The two MODIS datasets were overlaid and two spectral reflectance study pixels with a spatial resolution of 250m were located in the same pixel of the cloud state layer (1km spatial resolution). Thus, the cloud state of the cloud state layer overlapping with spectral reflectance pixel 1 (see Fig. 5) was considered as that of the whole study area. Then, the cloud mask was developed using the information contained in the 16 packed quality bits found in the cloud state layer. The first three of the available 16 bits were applied to develop the cloud mask that excluded pixels with clouds and cloud shadows (Table 1). Consequently, all the cloudy pixels were masked out from spectral reflectance dataset.

Table 1. MODIS surface reflectance QA science dataset bits used to mask out cloudy data.

| **Bit position** | **Bit description** | **Bit value accepted as cloud-free data** |
|---|---|---|
| 0 and 1 | Cloud state | "00" (clear) |
| 2 | Cloud shadow | "0" (no cloud shadows) |

2.2.2 Flagging flooded and non-flooded pixels within the cloud-free MODIS spectral reflectance dataset

In this thesis, a derived metric (called "water percentage") from PhenoCam data was used to identify whether the vegetated marshes in the study pixels were tidally inundated. The metric was developed by collaborators in my working group (O'Connell & Alber, in preparation). Red green and blue (RGB) values were extracted from each available PhenoCam image. Each image pixel was classified based on the RGB color space using custom scripts in the R program for statistical analysis. This classification was used to derive weather conditions, tidal inundation and other ancillary data, including percent of vegetated marsh which was flooded (O'Connell and

Alber, unpublished data). To derive this classification, PhenoCam images, which are archived as jpegs, were decompressed and digital numbers corresponding to the brightness levels in the red-green-blue (RGB) color space were extracted. A CLARA (Clustering for LARge Applications) analysis (Kaufman & Rousseeuw, 2009) (package "cluster" in R) was applied to perform an unsupervised classification across representative PhenoCam images. From these, a library of color clusters for common objects, such as water vs. vegetation, was developed. This library was used to refine the unsupervised classification into a "smart classifier" that accounted for differing color characteristics of objects under bright vs. cloudy conditions.

Using the PhenoCam timestamps, MODIS fly over times were matched with their corresponding ground based observations. MOD11A1 is a MODIS/Terra land surface temperature and emissivity product. It is gridded in the sinusoidal projection and produced daily with a spatial resolution of 1 km. It also provides the MODIS day viewing time that is stored in the layer "*Day_view_time*" (hereafter the "view time layer"). The view time stored in this layer was the apparent solar time (*AST*), which was based on the sun's actual position in the sky (Kurths & Herzel, 1987). Thus, the *AST* needed to be transformed to local standard time (*LST*) the time format in PhenoCam data. In this step, the method proposed by Holbert (2007) was applied to calculate the *LST* based on *AST*. The formulas are as below:

$$LST = AST - EoT - 4\ (min/deg) * (LSTM - Long) \quad (1)$$

Where *LST* is the local standard time;

*AST* is the apparent solar time;

*Long* is the local longitude at the position of interest;

*LSTM* is the local longitude of standard time meridian,

$$LSTM = 15° * \left(\frac{Long}{15°}\right)_{round\ to\ integer} \quad (2)$$

*EoT* is the equation of time;

$$EoT = 9.87 \sin(2D) - 7.53 \cos(D) - 1.5 \sin(D) \quad (3)$$

Where *D* is a transformation of the number of days since Jan 1 of the year (*doy*),

$$D = (2\pi/365) * (doy-81) \quad (4)$$

Next, PhenoCam-derived percent water was merged with the MODIS spectral reflectance dataset for each day. To accomplish this, it was necessary to know which PhenoCam image corresponded to Terra local view time. The orbit of MODIS platform Terra around the Earth is scheduled to pass from North to South across equator at about 10:30 am (Neteler, 2005). MODIS Terra usually views the earth's surface between 10:00am and 12:00pm (local standard time). Therefore, it was used only that PhenoCam images corresponding to the time window from 10:00am to 12:00pm. As a result, there were five relative time points with corresponding PhenoCam images (at 10:00am, 10:30am, 11:00am, 11:30am, and 12:00pm) in each day since the PhenoCam data were captured every half hour. For most MODIS pixels, view times could be determined (hereafter "pixels with view time"). Then, the water percentage of the nearest PhenoCam image acquisition that occurred when MODIS passed was used to represent that of the MODIS image. The water percentage of the earlier time point was used when the local view time had two nearest time points (such as 11:15am). However, several MODIS pixels did not have the view time information (stored as "not available"). The water percentage values of the five time points from the same day were used to determine the flood status of these pixels (hereafter called "pixels without view time") as described in the next paragraph. As a result, the MODIS pixels had either one or five water percentage values for each day.

Finally, the water percentage values of MODIS pixels were used to discriminate whether marsh vegetation within the pixels was flooded or not. A variable named *flood status* was created

to represent the flood status of the marsh vegetation. Flood status was either "not flooded" (*flood status* = 0), "flooded" (*flood status* = 1) or "unknown" (*flood status* = 2). The "unknown" status was necessary for pixels lacking of enough information to determine the flood status of the marsh vegetation. The next step was to set the rules to derive the values of *flood status* based on water percentage values. A very low cut-off water percentage value (2%) was used to define non-flooded condition to ensure the low uncertainty of dry marsh vegetation. There were visually seen water in the PhenoCam images with water percentage values larger than 6. As shown in Fig. 7, if the water percentage was smaller than 2 (i.e., less than 2 % of PhenoCam pixels were classified as water), the vegetated marsh was not flooded (see Fig. 7a and 7b); if the water percentage was larger than 6, the vegetated marsh was flooded (Fig. 7e and 7f); but if the water percentage value was between 2 and 6, the vegetated marsh flood status was unknown (see Fig. 7c and 7d). Therefore, for pixels with view time, the *flood status* values were set according to the above rules. But for pixels without view time, several rules were employed to assign a probable flood status. If the maximum water percentage between 10:00 am and 12:00 am (five time points) was smaller than 2, the *flood status* was assigned to 0 (not flooded); if the minimum water percentage within the time window was larger than 6, the *flood status* was assigned to 1 (flooded). Otherwise, *flood status* was assigned to 2 (unknown). As a result, the MODIS data had the *flood status* metric for each day. For all subsequent analyses, observations with a flood status of "unknown" were omitted.

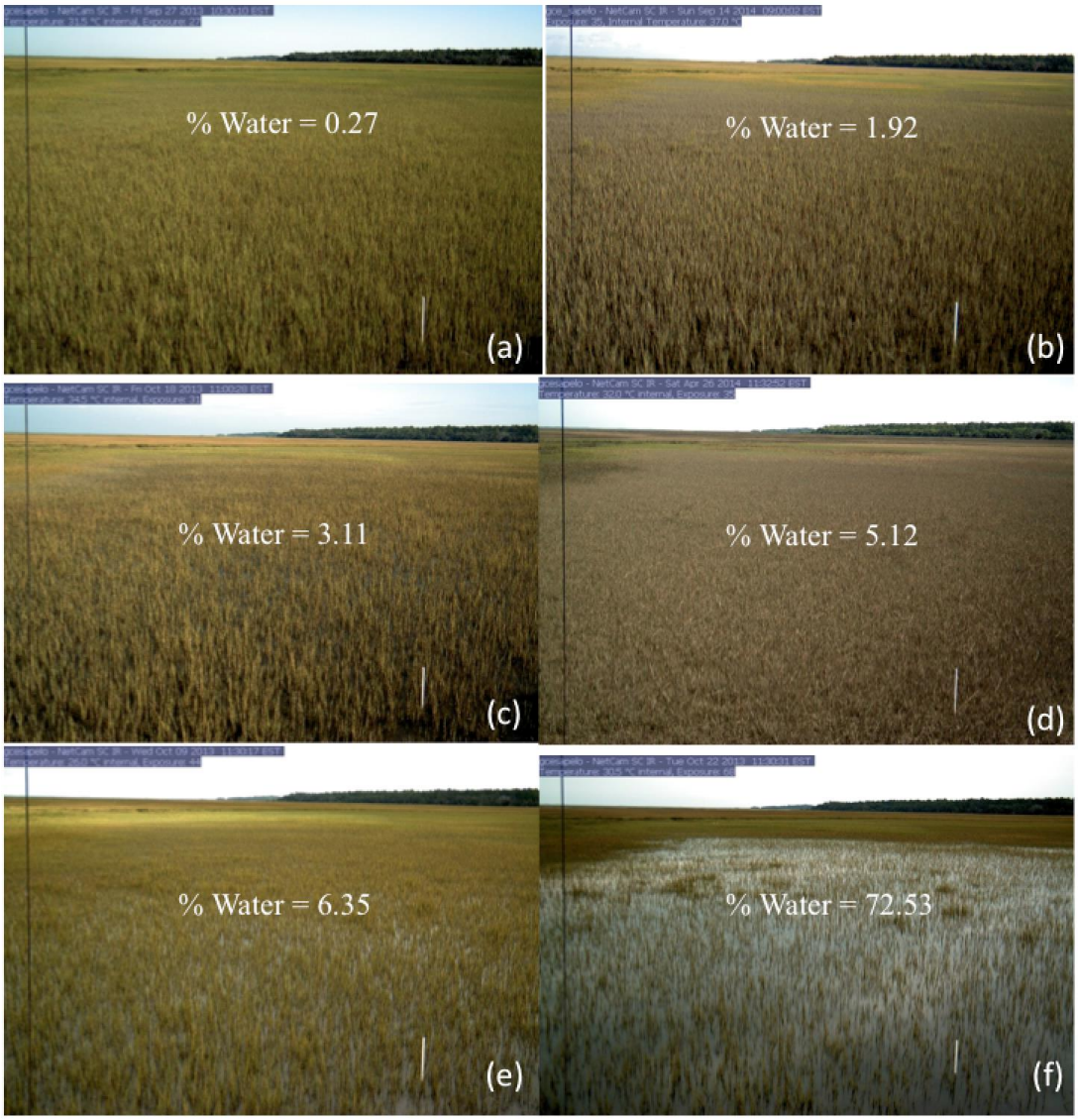


Figure 7. PhenoCam images with different water percentages as derived from classification of the RGB color space within each image. The percentage water of a and b were 0.27 and 1.92 respectively (not flooded); the percentage water of c and d were 3.11 and 5.12 respectively (unknown); and the percentage water of e and f were 6.35 and 72.53 respectively (flooded).

**2.3 Developing a classifier to separate MODIS cloud-free images as flooded and non-flooded**

In this section, logistic regression was used to develop a model which evaluated the probability that an observation could be classified as flooded. The dataset to build the model

consisted of cloud-free images with *flood status* of 0 or 1 from 2013-09-16 to 2014-12-31 (hereafter called "training dataset"). After building the model, cross-validation was applied to this training dataset to assess how well the results of model would generalize to an independent data set. Then, cloud-free images with *flood status* of 0 or 1 from 2015-01-01 to 2015-05-31 (hereafter called "testing dataset") were used to test the model applicability over different time period.

Logistic regression is a type of probabilistic statistical classification method. It measures the relationship between the categorical dependent variable and one or more independent variables, which are usually (but not necessarily) continuous, by estimating probabilities (Freedman, 2009). Put another way, logistic regression predicts a response variable from one or more predictor variables by using probability scores as the predicted values of the dependent variable (Walker & Ducan, 1967). The advantage of logistic regression is that the variables may be either continuous or discrete, or any combinations of both types and they do not necessarily have normal distributions. This contrasts with linear regression models, where model residuals must be normally distributed. In addition, in the case of linear discriminant analysis, a commonly used statistic classification model, the independent variables must have normal distributions (Atkinson & Massari, 1998), limiting its use for some kinds of data. In the present situation, the dependent variable is a binary variable representing whether the vegetated marsh is tidally flooded or not. Therefore, the logistic regression was used to build the classification model.

The *flood status* was applied as response variable and surface reflectance of red and near-infrared spectrums as predictors of the logistic regression classification model (Section 2.3.1). As Fig. 8 shown, there were phenology patterns of NDVI and WDRVI of cloud-free MODIS images. Therefore, it was necessary to check if the classification model was improved after

adding phenology variables to the model, capturing variation due to phenology and removing it from error terms. Hence, the model with phenology predictor for an entire year was developed in Section 2.3.2.

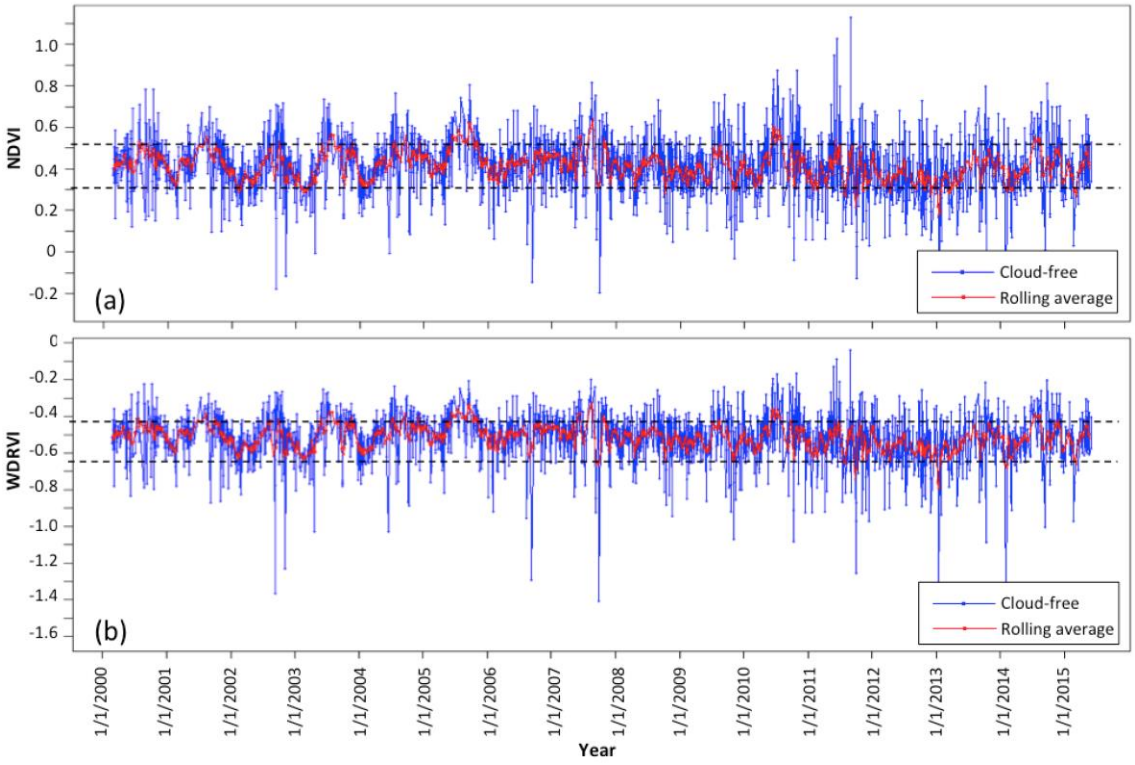


Figure 8. NDVI (a) and WDRVI (b) values of MODIS cloud-free pixels acquired in section 2.2.1 and rolling averages by eight days.

2.3.1 Building the logistic regression model with predictors of red and NIR reflectance

To build the classification model, a model selection function in R, called "step", was used to do stepwise logistic regression first. This procedure preforms stepwise addition (when starting with the null model) or deletion (when starting with the full model) of terms from a list of candidates for inclusion. Selection of terms for deletion or inclusion is based on Alaike's information criterion (AIC) (Hastie & Pregibon, 1992). The lower the AIC is, the better the model fit. Here, model selection started with the full model (i.e. all interaction terms included). The final best logistic regression model formula was as below:

$$flood\ status \sim \rho_r + \rho_{NIR} \quad (5)$$

Where *flood status* was the binary response variable, as defined in Section 2.2.2. $\rho_r$ was the surface reflectance of the MODIS red band and $\rho_{NIR}$ was the surface reflectance of the MODIS near-infrared band.

After model building, the explained deviance was used to evaluate the goodness of model fit. Logistic regression models do not have quite the same properties as linear regression models such as $R^2$. But analogous to $R^2$, explained deviance (1-(residual deviance/null deviance)) is a good indicator of overall model fit (Braak & Tongeren, 1995). The larger the explained deviance is, the better the model fit.

2.3.2 Building the logistic regression model with predictors of phenology patterns variable, red and NIR reflectance for an entire year

In order to include phenology variable as a predictor of the model, it first should be described by a mathematical function. NDVI and WDRVI were used to derive the phenology patterns variable respectively. As shown in Fig. 8, phenology patterns are regular repeating curves. Such curves might be described mathematically using the cosine as a function of the day of year (Equation 6) (Matthiopoulos, 2013).

$$f(doy) = a * cos\ (2 * \pi / TP * (doy - d_0)) + b \quad (6)$$

Where *f(doy)* was the variable that represented phonology patterns (Hereafter, it was named $T_{NDVI}$ if derived from NDVI patterns (Fig. 8a) or $T_{WDRVI}$ if derived from WDRVI patterns (Fig. 8b)). *doy* was the day of year. *TP* was time period circle of cosine function and equaled the number of days of one year. $d_0$ horizontally shifted the cosine peak to the day when NDVI (WDRVI) was the highest. *b* vertically shifted the cosine peak to the highest NDVI (WDRVI). *a* was the amplitude of cosine function.

Specifically, to derive these coefficients in Equation 6, rolling averages of NDVI (Fig. 8a) and WDRVI (Fig. 8b) by eight days were calculated for MODIS cloud-free pixels in the dataset across 2000 to 2015 and the following calculations were based on rolling averages instead of original dataset. Then, the averages of top five maximal and minimal NDVI (WDRVI) of each year were calculated respectively, named *maximal NDVI (WDRVI)* and *minimal NDVI (WDRVI).* Also, the days when the top five maximal NDVI (WDRVI)s occurred were averaged for each year, named *peak NDVI*(*WDRVI*). Then, the averages of these six variables of 15 years were calculated as final maximal NDVI (WDRVI), minimal NDVI (WDRVI), and peak NDVI (WDRVI) respectively, which were used to derive the coefficients in Equation 6. *a* equaled half of difference of maximal and minimal NDVI (WDRVI). *b* equaled the difference of maximal NDVI (WDRVI) and corresponding *a* value. $t_0$ equaled the peak NDVI (WDRVI). As a result, $T_{NDVI}$ and $T_{WDRVI}$ were calculated from Equation 6 for each MODIS images within the training and testing dataset.

To build the logistic regression model with three predictors including red reflectance ($\rho_r$), NIR reflectance ($\rho_{NIR}$) and phenology variable ($T_{NDVI}$ or $T_{WDRVI}$) for an entire year, stepwise logistic regression was ran in R to select the final best model formula (Equation 7). Then, the probability that an observation could be classified as flooded was predicted based on the best logistic regression model. Also, it was necessary to set a cut-off probability value (called "cp") to get the binary predicted categories (flooded or non-flooded). Here, sensitivity analysis was used to select the most appropriate cp value. Specifically, the range of cp was 0 to 1 and the incremental interval was 0.01 so that there were 100 cp values as candidates. The purpose of this thesis is to identify and filter out MODIS data when tidal influence is dominant in salt marsh vegetation. Thus, it is important that the cut-off be conservative for identifying dry marsh and

there should be low uncertainty that pixels classified as non-flooded have high correspondence with true observations. For flooded marsh classifications, uncertainty can be greater because the purpose of this analysis is to filter any marsh pixels that have some realistic probability of being flooded from the data. Therefore, the classification error that should be mostly reduced is the misclassification of true flooded pixels as non-flooded. Therefore, the selection of cp value was to maximize both the overall classification accuracy and non-flooded classification accuracy. Finally, the best cp was applied as cut-off probability to classify observations as flooded and non-flooded.

$$flood\ status \sim \rho_r + \rho_{NIR} + T_{NDVI}\ (\text{or } T_{WDRVI}) \quad (7)$$

After the model building, cross-validation was used to evaluate the model. Cross-validation is a model evaluation method that gives an indication of how well the model will perform when it is used to make new predictions for data it has not already seen (Efron, 1983). The purpose of cross-validation is to avoid overfitting problems of the model. Overfitting means a model has a perfect score in the training dataset but will fail to predict anything useful on yet-unseen data (Kohavi, 1995). Since one of applications of this model is to do predict the flood status of MODIS cloud-free images before 2013, it was necessary to use cross-validation to evaluate the model. Specifically, the entire training dataset was divided into five subsets and the logistic regression classification model was repeated 100 times. Each time, one of the five subsets was used as test set and the other four subsets were put together to form a training set for cross-validation. After 100 times computing, it was calculated that average overall classification accuracy with a corresponding root mean square error (RMSE) and average non-flooded classification accuracy with a corresponding RMSE.

The classification model was applied to the testing dataset to test the model applicability over a different time period. First, the probability that MODIS images could be classified as flooded was predicted for the testing dataset. Then, the best cut-off probability (cp) was used to classify the dataset as non-flooded and flooded. Finally, a classification confusion table was made and overall classification accuracy and non-flooded classification accuracy were calculated by comparing the predicted results with the actual flood status that was derived from PhenoCam images.

### 2.4 Developing a tide adjusted wetland index (TAWI) based on the results of logistic regression model

The results of logistic regression model derived in Section 2.3.2 were used to develop TAWI that could be applied to identify the non-flooded data within cloud-free MODIS images. Although the logistic classification model can be used to predict flood status of MODIS images, it is not easy and straightforward to be practically performed if users are not familiar with this statistical method. Consequently, it was necessary to derive an index, TAWI, which could be calculated by a simple equation to simplify the model.

The logistic function (Equation 8) was introduced to explain how to derive TAWI from the logistic regression model. The logistic function can take an input with any value from negative to positive infinity, whereas the output always takes values between zero and one and hence is interpretable as a probability (Zuur et al., 2009). TAWI equaled the probability of observations that could be classified as flooded ($P(\gamma)$). Then, if TAWI was smaller than the selected cut-off probability, the observation would be classified as non-flooded; Otherwise, if TAWI was larger than or equal to the cut-off probability, the observation would be classified as flooded.

$$TAWI = P(\gamma) = \frac{1}{1+e^{-\gamma}} \quad (8)$$

Where $P(\gamma)$ is the probability of the observations that can be classified as the class coded by 1;

$$\gamma = \beta_0 + \beta_1 * V_1 + \beta_2 * V_2 + \ldots + \beta_n * V_n \quad (9)$$

Where $V_1, V_2, \ldots, V_n$ are the independent variables in the logistic regression model;

$\beta_1, \beta_2, \ldots, \beta_n$ are corresponding regression coefficients of variables;

$\beta_0$ is the intercept of the logistic regression model.

**2.5 Applying tide adjusted wetland index (TAWI) to identify the non-flooded vegetation within MODIS cloud-free dataset**

One of the significant applications of TAWI was to identify the non-flooded vegetation within MODIS cloud-free images of the study area from 2000 to 2015. First, TAWI values were calculated using Equation 8 and 9. Then, the MODIS dataset was classified as flooded and non-flooded based on the cut-off probability derived in Section 2.3. As a result, the entire MODIS cloud-free images were filtered to the non-flooded dataset. To be clear, what I called the non-flooded dataset in the following analysis was generated within MODIS cloud-free dataset.

Further, TAWI could be used to predict the flood status of satellite cloud-free images in a different place as well as broader area. But it requires satellite images have a high temporal resolution due to the high temporal variation of tide inundation. It also requires the places to be predicted have similar phenology patterns to the study site, such as the peak day, growing season and non-growing season. Thus, the flood status of three salt marsh sites (Table 2 and Fig. 9), in Georgia, South Carolina and North Carolina respectively which have similar phenology patterns to the study site, was predicted using TAWI that calculated by MODIS daily reflectance dataset from 2000 to 2015. These three salt marshes are all influenced by the tide effect to different degrees. The tide is highest in Georgia salt marshes and lowest in North Carolina salt marshes.

Table 2. The locations of three salt marshes that were predicted the flood status using TAWI

| Position No. | Position name | Latitude | Longitude |
|---|---|---|---|
| 1 | Pine Harbor, Sapelo River, GA | 31.55N | 81.37W |
| 2 | Garden City Bridge, Main Creek, SC | 33.58N | 79.00W |
| 3 | Southport, NC | 33.91N | 78.03W |

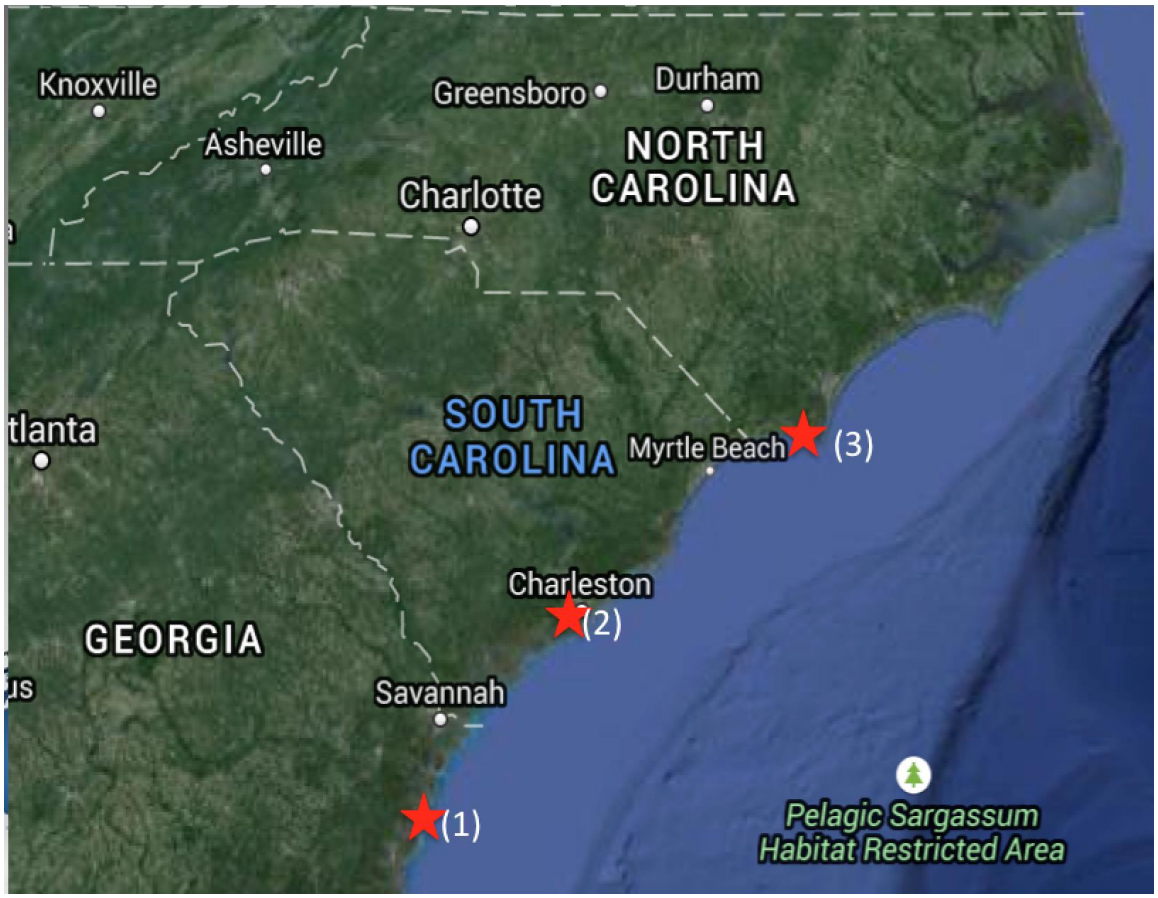


Figure 9. Map of three salt marsh sites. The stars represented the locations where the flood status was predicted using TAWI. The names and locations of these three sites were presented in Table 2.

CHAPTER 3

RESULTS

### 3.1 MODIS images with flooded and non-flooded flags

The MODIS daily surface reflectance products used for this analysis were from 2000-02-24 to 2015-05-31. After applying the cloud mask, the average number of images remaining each year was 135.9 ±4.1 (mean ± S.E.) out of an average of 365.2 total images acquired per year (Fig. 10). Since the MODIS images of 2000 and 2015 didn't cover the entire year, the average was acquired from 2001 to 2014. Across years, the cloud mask removed 62.8% ∓1.1% (mean ∓ S.E.) of MODIS images, leaving 37.2% ± 1.1% (mean ± S.E.) data for analysis (365.2 images total).

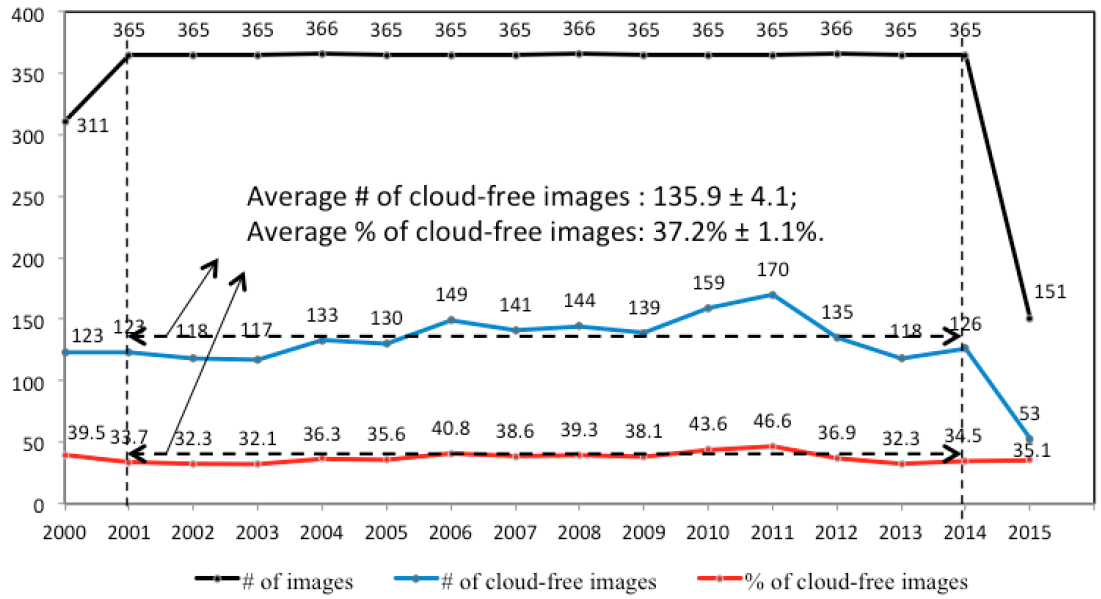


Figure 10. The number (#) of MODIS images, the number (#) and percentage (%) of MODIS cloud-free images by year (2000-2015). The average # and % of cloud-free images were 135.9 ± 4.1 (mean ± S.E.) and 37.2% ± 1.1% (mean ± S.E.) respectively for 2001-2014.

The MODIS could-free images (2013-09-16 to 2015-05-31) were flagged with three categories, non-flooded, flooded and unknown vegetated marsh using the metric water percentage derived from PhenoCam images. As a result, 64% of the MODIS cloud-free images were non-flooded and 15% were flooded (214 images total) (Fig. 11a). However, there were still 21% unknown flooded status images, a greater category than the flooded images. There were 16 flooded observations and 89 non-flooded observations in non-growing season (1/1-4/14 & 11/1-12/31). And there were 16 flooded observations and 48 non-flooded observations in growing season (4/15-10/31). Thus, growing season has less non-flooded observations than non-growing season (Fig. 11b).

As shown in the table of Fig. 11, the averages of red reflectance of non-flooded observations in growing season and non-growing season were 0.05 ± 0.02 (mean ± S.D.) and 0.04 ± 0.01 (mean ± S.D.) respectively. The averages of red reflectance of flooded observations in growing season and non-growing season were 0.04 ± 0.02 (mean ± S.D.) and 0.04 ± 0.01 (mean ± S.D.) respectively. The averages of near-infrared reflectance of non-flooded observations in growing season and non-growing season were 0.13 ± 0.04 (mean ± S.D.) and 0.11 ± 0.03 (mean ± S.D.) respectively. The averages of near-infrared reflectance of flooded observations in growing season and non-growing season were 0.09 ± 0.03 (mean ± S.D.) and 0.08 ± 0.03 (mean ± S.D.) respectively. The average near-infrared reflectance of non-flooded was significantly larger than flooded group in growing season, with a t value of 4.26 and p value of 0.000. Also, the average near-infrared reflectance of non-flooded was significantly larger than flooded group in non-growing season, with a t value of 3.34 and p value of 0.003. However, the average of red reflectance of non-flooded observations was not significantly different from that of flooded in growing season or non-growing season with p values larger than 0.05.

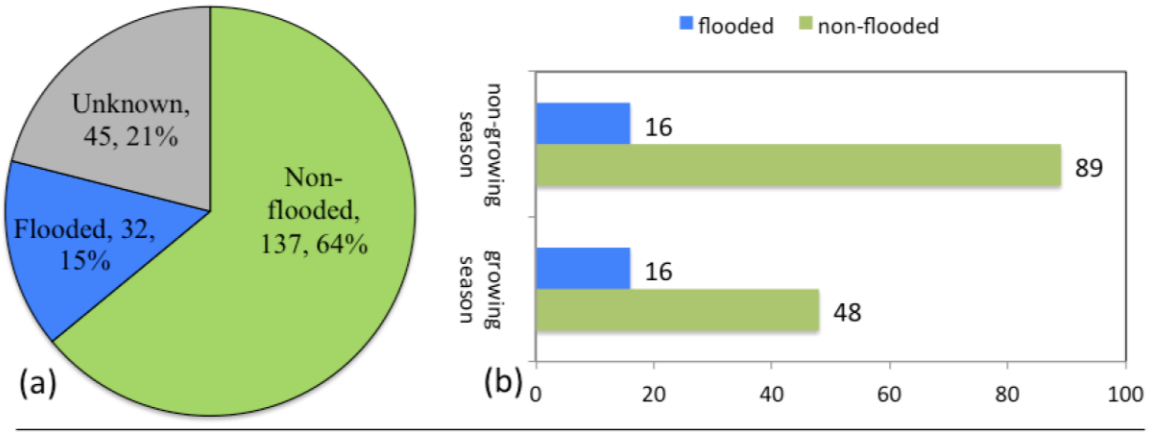


| | | Red | | Near-infrared (nir) | |
|---|---|---|---|---|---|
| **Flood status** | **Time period** | **Mean** | **S.D.** | **Mean** | **S.D.** |
| Non-flooded | Growing season | 0.05 | 0.02 | 0.13 | 0.04 |
| | Non-growing season | 0.04 | 0.01 | 0.11 | 0.03 |
| Flooded | Growing season | 0.04 | 0.02 | 0.09 | 0.03 |
| | Non-growing season | 0.04 | 0.01 | 0.08 | 0.03 |

[a]t-test for difference of mean red reflectance between non-flooded and flooded in growing season: t = 0.74; p = 0.467.
[b]t-test for difference of mean nir reflectance between non-flooded and flooded in growing season: t = 4.26; p = 0.000.
[c]t-test for difference of mean red reflectance between non-flooded and flooded in non-growing season: t = 0.48; p = 0.635.
[d]t-test for difference of mean nir reflectance between non-flooded and flooded in non-growing season: t = 3.34; p = 0.003.

Figure 11. (a) The number and percentage of flooded, non-flooded and unknown flood status MODIS cloud-free images classified via PhenoCam derived flood metrics across the time period of 2013-09-16 to 2015-05-31. (b) The number of flooded and non-flooded MODIS cloud-free images by growing and non-growing season. The insert table was mean and standard deviation (S.D.) of red and near-infrared surface reflectance values by flood status and time periods.

### 3.2 The classifier separating MODIS cloud-free images as flooded vs. non-flooded

3.2.1 Results of logistic regression model with predictors of red and NIR reflectance

The MODIS cloud-free images were classified into two categories, flooded and non-flooded based on the logistic regression classification model with predictors of red and NIR reflectance. This model explained 21.7 % of the variation in flood status of the vegetated marsh

(explained deviance = 21.7%). The logistic regression coefficients give the change in the log odds of the outcome for one unit increase in the predictor variable. Here, the coefficients of two predictors of the model were 54.0 and -54.3 for red and NIR reflectance respectively, indicating the log odds of probability that a pixel was flooded increased by 54.0 for one unit change in red reflectance and decreased by 54.3 for one unit change in near-infrared reflectance (Table 2). As mentioned before, the model predicted the probability that an observation could be classified as flooded. Hence, the red reflectance had a positive relationship with the probability of flooded while the near-infrared reflectance had a negative one.

Table 3. Summary of logistic regression classification model with predictors of red and NIR reflectance for predicting the probability of MODIS image as flooded.

| **Predictor** | **Coefficient** | **Standard error** | **Z value** | **P value** |
|---|---|---|---|---|
| *Intercept* | 1.3 | 0.9 | 1.4 | 0.148 |
| $\rho_r$ | 54.0 | 22.3 | 2.4 | 0.015* |
| $\rho_{NIR}$ | -54.3 | 13.9 | -3.9 | 0.000*** |

[a]Explained deviance = 1 – (residual deviance/null deviance) = 1 – 93.5/119.4 = 21.7%

[b]* p<0.05; ** p<0.01; *** p<0.001.

3.2.2 Results of logistic regression model with predictors of red, NIR reflectance and phenology variable ($T_{nNDVI}$ or $T_{WDRVI}$)

As mentioned in Section 2.3.2, $T_{NDVI}$ and $T_{WDRVI}$ were two phenology variables deriving from NDVI and WDRVI patterns respectively. The coefficients of $T_{NDVI}$ were 0.11 for *a*, 0.42 for *b*, 365 for *TP* and 220 for $d_0$ (Equation 6). The coefficients of $T_{WDRVI}$ were 0.12 for *a*, -0.56 for *b*, 365 for *TP* and 218 for $d_0$ (Equation 6). The peak days $d_0$ of two phenology variables were both in August (220: August 8; 218: August 6). The logistic regression classification model with the phenology patterns predictor derived by NDVI patterns (hereafter called "$LRM_{NDVI}$") explained

29.6% of the variation in flood status of the vegetated marsh (explained deviance = 29.6%). The coefficients of three predictors of the model were 63.9 for red reflectance, -66.9 for NIR reflectance and 13.3 for $T_{NDVI}$ respectively, indicating the log odds of probability that a pixel was flooded increased by 63.9 for one unit change in red reflectance, decreased by 66.9 for one unit change in near-infrared reflectance and increased by 13.3 for one unit change in $T_{NDVI}$ (Table 4). On the other hand, the logistic regression classification model with the phenology patterns predictor derived by WDRVI patterns (hereafter called "$LRM_{WDRVI}$") also explained 29.6% of the variation in flood status of the vegetated marsh (explained deviance = 29.6%). The coefficients of three predictors of the model were 63.7 for red reflectance, -67.1 for NIR reflectance and 12.3 for $T_{WDRVI}$ respectively, indicating the log odds of probability that a pixel was flooded increased by 63.7 for one unit change in red reflectance, decreased by 67.1 for one unit change in near-infrared reflectance and increased by 12.3 for one unit change in $T_{WDRVI}$ (Table 4). Hence, the red reflectance and phenology patterns variable had a positive relationship with the probability of flooded while the near-infrared reflectance had a negative one for both $LRM_{NDVI}$ and $LRM_{WDRVI}$.

Table 4. Summary of logistic regression classification model, $LRM_{NDVI}$ and $LRM_{WDRVI}$, for predicting the probability of MODIS image as flooded.

| **Model** | **Predictor** | **Coefficient** | **Standard error** | **Z value** | **P value** |
|---|---|---|---|---|---|
| $LRM_{NDVI}$ | *Intercept* | -3.3 | 1.8 | -1.8 | 0.066 |
| | $\rho_r$ | 63.9 | 22.5 | 2.8 | 0.005 ** |
| | $\rho_{NIR}$ | -66.9 | 16.2 | -4.1 | 0.000 *** |
| | $T_{NDVI}$ | 13.3 | 4.6 | 2.9 | 0.004 ** |
| $LRM_{WDRVI}$ | *Intercept* | 9.2 | 2.9 | 3.1 | 0.002 ** |
| | $\rho_r$ | 63.7 | 22.6 | 2.8 | 0.005 ** |
| | $\rho_{NIR}$ | -67.1 | 16.2 | -4.1 | 0.000 *** |

| | | | | |
|---|---|---|---|---|
| $T_{WDRVI}$ | 12.3 | 4.3 | 2.9 | 0.004 ** |

[a] $LRM_{NDVI}$ Explained deviance=1-(residual deviance/null deviance)=1-84.0/119.4=29.6%

[b] $LRM_{WDRVI}$ Explained deviance=1-(residual deviance/null deviance)=1-84.0/119.4=29.6%

[c] * p<0.05; ** p<0.01; *** p<0.001.

The overall accuracy of classification first increased to almost 90% and then fluctuated between 80% and 90% with the increasing of cut-off probability (cp) (Fig. 12). Instead, the non-flooded classification accuracy decreased with the increasing of cp and it was between 80% and 100%. Hence, the two accuracies could not be maximized at the same time and the appropriate balance point should be the best cp. Here, overall classification accuracy was ensured larger than 80% and then selected cp for $LRM_{NDVI}$ *(*$LRM_{WDRVI}$*)* that had the largest non-flooded classification accuracy. As a result, the best cp for $LRM_{NDVI}$ was 0.21, with the overall accuracy of 84.0% and non-flooded classification accuracy of 95.6%. And the best cp for $LRM_{WDRVI}$ was also 0.21, with the overall accuracy of 83.2% and non-flooded classification accuracy of 95.5%.

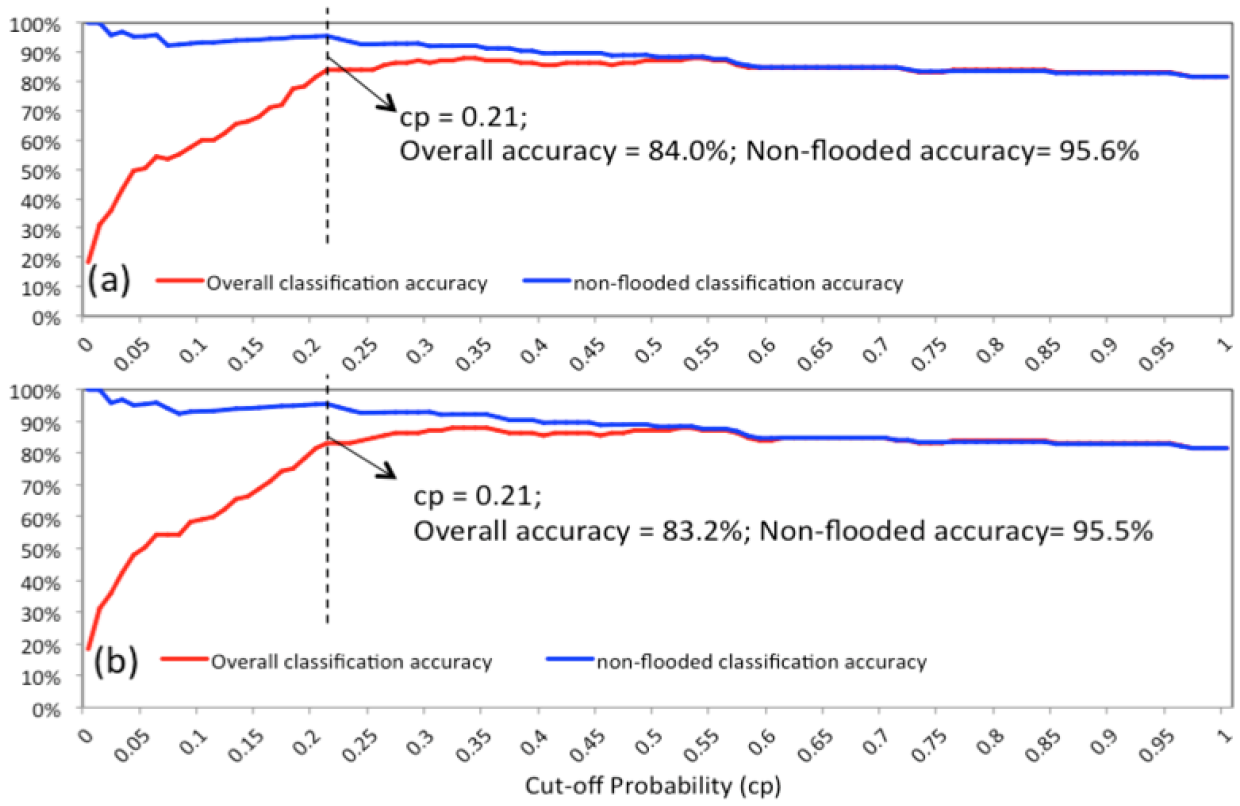


Figure 12. The overall and non-flooded classification accuracy based on the results of the logistic regression model for an entire year, (a) $LRM_{NDVI}$ and (b) $LRM_{WDRVI}$. These patterns change along with an increase in cut-off probability ("cp") for classifying observations as flooded. The best cp was (a) 0.21, with the overall accuracy of 84.0% and non-flooded accuracy of 95.6%; (b) 0.21, with the overall accuracy of 83.2% and non-flooded accuracy of 95.5%.

Based on the best cp for $LRM_{NDVI}$, 86 non-flooded and 19 flooded observations were classified correctly (Table 5). But there were 4 flooded observations misclassified as non-flooded observations and 16 non-flooded observations were misclassified as flooded. Five-fold cross validation showed the average overall classification accuracy was 77.0% ± 8.0% (mean ± RMSE) and non-flooded classification accuracy was 91.7% ± 6.7% (mean ± RMSE). Based on the best cp for $LRM_{WDRVI}$, 85 non-flooded and 19 flooded observations were classified correctly (Table 5). But there were 4 flooded observations misclassified as non-flooded observations and

17 non-flooded observations were misclassified as flooded. Five-fold cross validation showed the average overall classification accuracy was 77.3% ± 8.0% (mean ± RMSE) and average non-flooded classification accuracy was 91.8% ± 6.4% (mean ± RMSE).

Table 5. The classification confusion table resulting from the logistic regression model, $LRM_{NDVI}$ and $LRM_{WDRVI}$, run across the training data.

| | | Predicted | | |
|---|---|---|---|---|
| **Model** | **Observed** | **Non-flooded** | **Flooded** | **Overall** |
| $LRM_{NDVI}$ | Non-flooded | 86 | 16 | |
| | Flooded | 4 | 19 | |
| | Accuracy | 95.6% | 54.2% | 84.0% |
| $LRM_{WDRVI}$ | Non-flooded | 85 | 17 | |
| | Flooded | 4 | 19 | |
| | Accuracy | 95.5% | 52.8% | 83.2% |

[a]$LRM_{NDVI}$: 5-fold Cross validation results: average overall accuracy was 77.0% and RMSE was 8.0%. Average non-flooded accuracy was 91.7% and RMSE is 6.7%.

[b]$LRM_{WDRVI}$: 5-fold Cross validation results: average overall accuracy was 77.3% and RMSE was 8.0%. Average non-flooded accuracy was 91.8% and RMSE is 6.4%.

The logistic regression classification models were applied to the testing dataset. As a result, the overall classification accuracy was 86.4% and non-flooded classification accuracy was 87.2% for $LRM_{NDVI}$ (Table 6). The overall classification accuracy was 86.4% and non-flooded classification accuracy was 87.2% for $LRM_{WDRVI}$ (Table 6).

Table 6. The classification confusion table resulting from the logistic regression model, $LRM_{NDVI}$ and $LRM_{WDRVI}$, run across the testing data.

| Model | Observed | Predicted | | Overall |
|---|---|---|---|---|
| | | Non-flooded | Flooded | |
| $LRM_{NDVI}$ | Non-flooded | 34 | 1 | |
| | Flooded | 5 | 4 | |
| | Accuracy | 87.2% | 80.0% | 86.4% |
| $LRM_{WDRVI}$ | Non-flooded | 34 | 1 | |
| | Flooded | 5 | 4 | |
| | Accuracy | 87.2% | 80.0% | 86.4% |

As shown in Table 5 and 6, there were 4 flooded observations in the training dataset and 5 flooded observations in the testing dataset misclassified as non-flooded using $LRM_{NDVI}$ or $LRM_{WDRVI}$. And the 9 error observations from $LRM_{NDVI}$ were the same as those from $LRM_{WDRVI}$. These misclassified observations would reduce the quality of MODIS non-flooded products. Therefore, it was necessary to understand the cause of misclassification (Table 7 and Fig. 13).

Table 7. The red, NIR reflectance and percentage (%) water of flooded observations that were misclassified as non-flooded based on $LRM_{NDVI}$ or $LRM_{WDRVI}$.

| Date | $\rho_r$ | $\rho_{NIR}$ | % Water | Image No. in Fig. 13 |
|---|---|---|---|---|
| 2013-11-04 | 0.05 | 0.12 | 47.6 | a |
| 2012-12-06 | 0.05 | 0.13 | 8.1 | b |
| 2014-05-17 | 0.03 | 0.10 | 69.9 | c |
| 2014-11-07 | 0.05 | 0.13 | 27.4 | d |

| | | | | |
|---|---|---|---|---|
| 2015-02-07 | 0.05 | 0.08 | 8.2 | e |
| 2015-02-20 | 0.04 | 0.09 | 63.7 | f |
| 2015-04-21 | 0.05 | 0.11 | 13.1 | g |
| 2015-04-23 | 0.05 | 0.15 | 6.3 | h |
| 2015-05-31 | 0.03 | 0.09 | 8.9 | i |

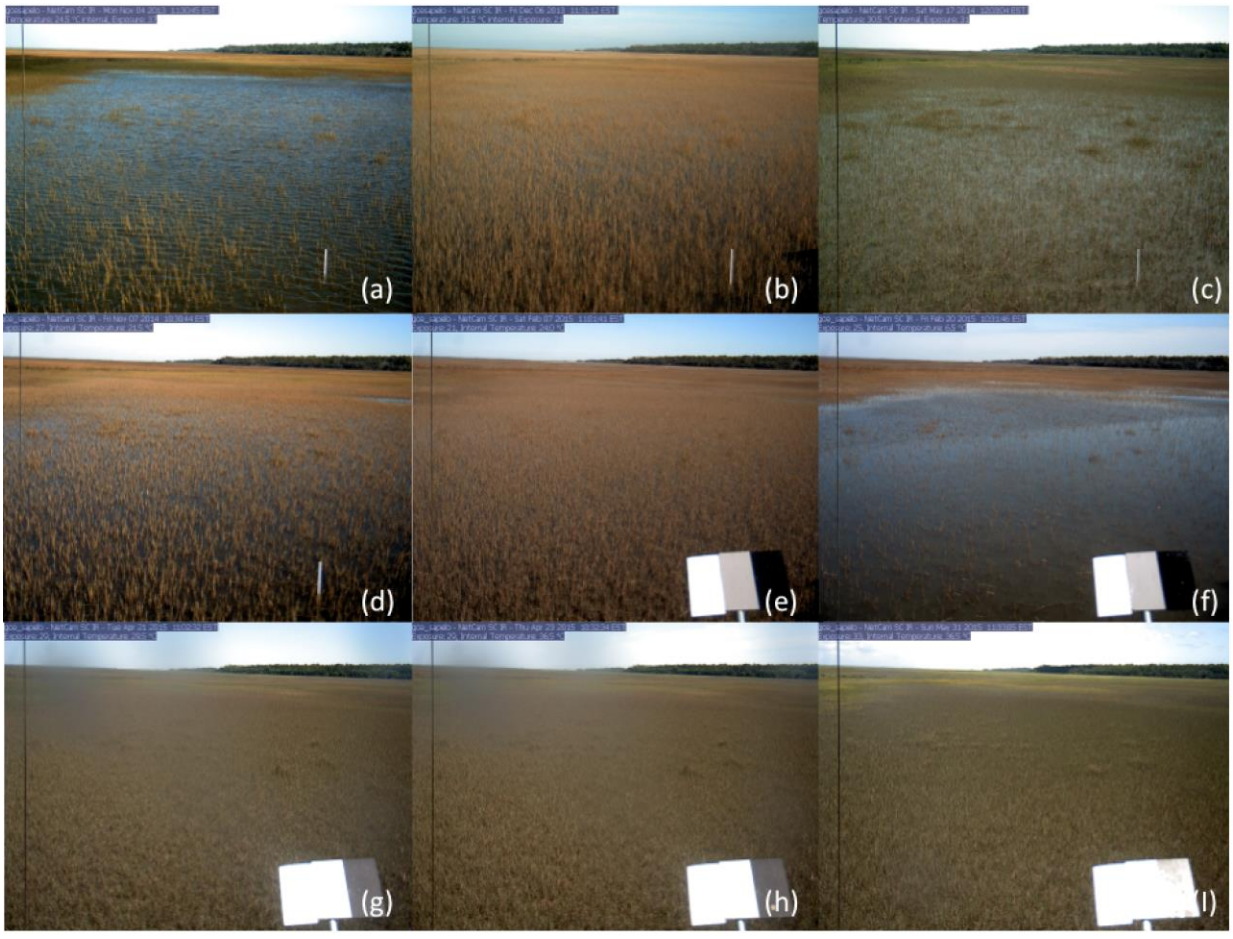


Figure 13. PhenoCam images of flooded observations that were misclassified as non-flooded. Image number a to i are related to the number in Table 7.

### 3.3 The tide adjusted wetland index (TAWI) for identifying the non-flooded images within MODIS cloud-free dataset.

For $LRM_{NDVI}$, the variables ($V_n$) of the model were $\rho_r$, $\rho_{nir}$, and $T_{NDVI}$ and the coefficients ($\beta_n$) of the variables were 63.9, -66.9 and 13.3 respectively. The intercept ($\beta_0$) of $LRM_{NDVI}$ was -3.3 (Equation 9). For $LRM_{WDRVI}$, the variables ($V_n$) of the model were $\rho_r$, $\rho_{nir}$, and $T_{WDRVI}$ and the coefficients ($\beta_n$) of the variables were 63.7, -67.1 and 12.3 respectively. The intercept ($\beta_0$) of $LRM_{WDRVI}$ was 9.2 (Equation 9). Consequently, the TAWI could be calculated by the surface reflectance of red ($\rho_r$) and NIR ($\rho_{NIR}$) and the day of year (*doy*) according to the Equations 6, 8 and 9. The resulting TAWI calculation equation is as below (Equation 10 and 11). And the cut-off values of $TAWI_{NDVI}$ and $TAWI_{WDRVI}$ were both 0.21.

$$TAWI_{ndvi} = \frac{1}{1+ e^{-63.9 * \rho_r + 66.9 * \rho_{NIR} - 1.5 * \cos(0.02 * doy - 3.7) - 2.3}} \quad (10)$$

$$TAWI_{wdrvi} = \frac{1}{1+ e^{-63.7 * \rho_r + 67.1 * \rho_{NIR} - 1.5 * \cos(0.02 * doy - 3.7) - 2.3}} \quad (11)$$

Where $TAWI_{NDVI}$ and $TAWI_{WDRVI}$ were the tide adjusted wetland index derived by $LRM_{NDVI}$ and $LRM_{WDRVI}$ respectively. $\rho_r$ is the surface reflectance of the MODIS red band. $\rho_{NIR}$ is the surface reflectance of the MODIS NIR band; and *doy* is the day of year.

### 3.4 The application of tide adjusted wetland index (TAWI) in generating the MODIS non-flooded products of 2000-2015

The NDVI rolling average (by eight days) plot (Fig. 14a) of non-flooded MODIS images (post-TAWI) in the study site was smoother and had more obvious phenology patterns than MODIS cloud-free images (pre-TAWI). The WDRVI rolling average (by eight days) plot (Fig. 14b) had similar patterns to NDVI. The phenology patterns were more fluctuated from 2006 than previous years, especially in 2011 and 2012.

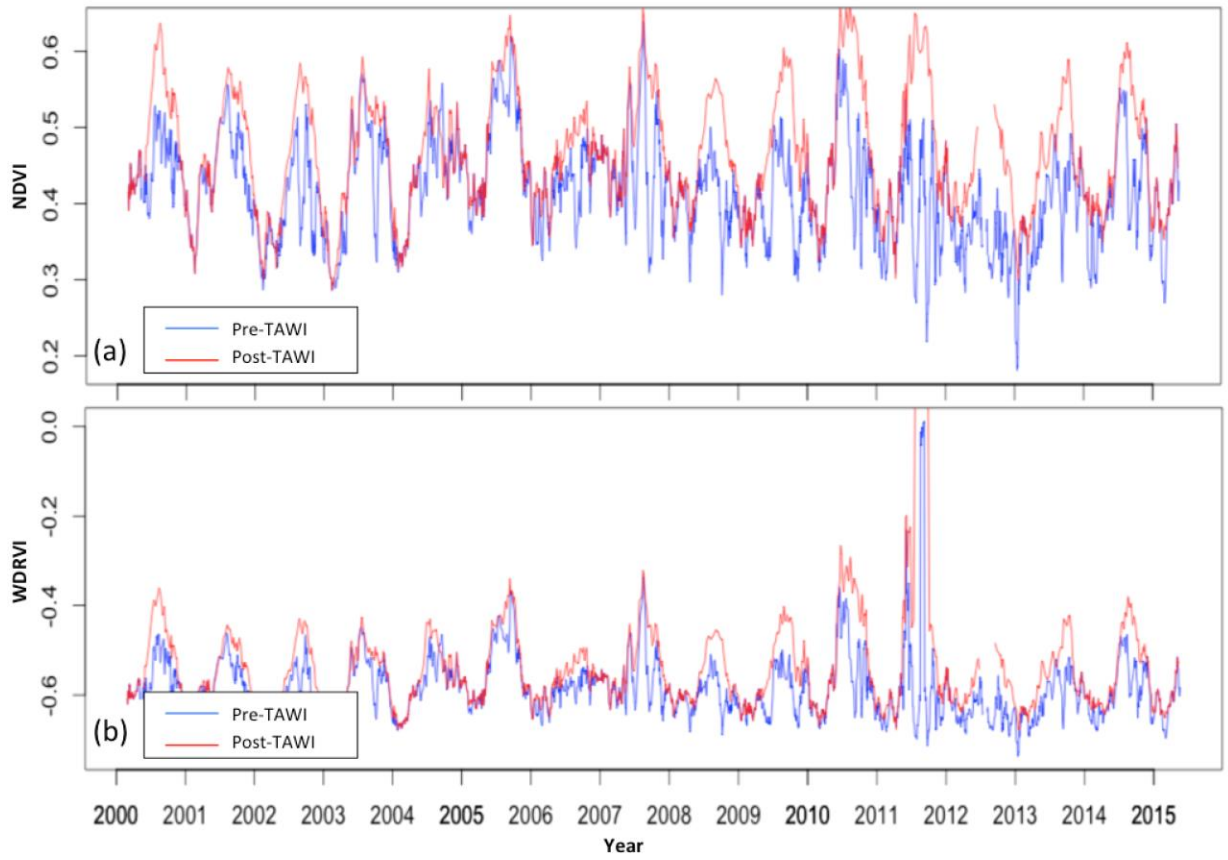


Figure 14. NDVI (a) and WDRVI (b) rolling averages (by eight days) of MODIS cloud-free pixels (pre-TAWI) and non-flooded pixels predicted by the TAWI (post-TAWI) in the study site (see Fig. 3).

For three salt marshes in Georgia, South Carolina and North Carolina, the NDVI rolling average (by eight days) plots (Fig. 15a, 16a and 17a) of non-flooded MODIS images (post-TAWI) were smoother and had more obvious phenology patterns than MODIS cloud-free images (pre-TAWI) respectively. The WDRVI rolling average (by eight days) plots (Fig. 15b, 16b, and 17b) had similar patterns to NDVI. It demonstrated that TAWI could identify non-flooded observations for these three salt marshes. In addition, the phenology patterns were more fluctuated from 2006 than previous years for the three sites. The phenology patterns of salt marsh in Georgia were the most fluctuated, followed by South Carolina, and then North Carolina.

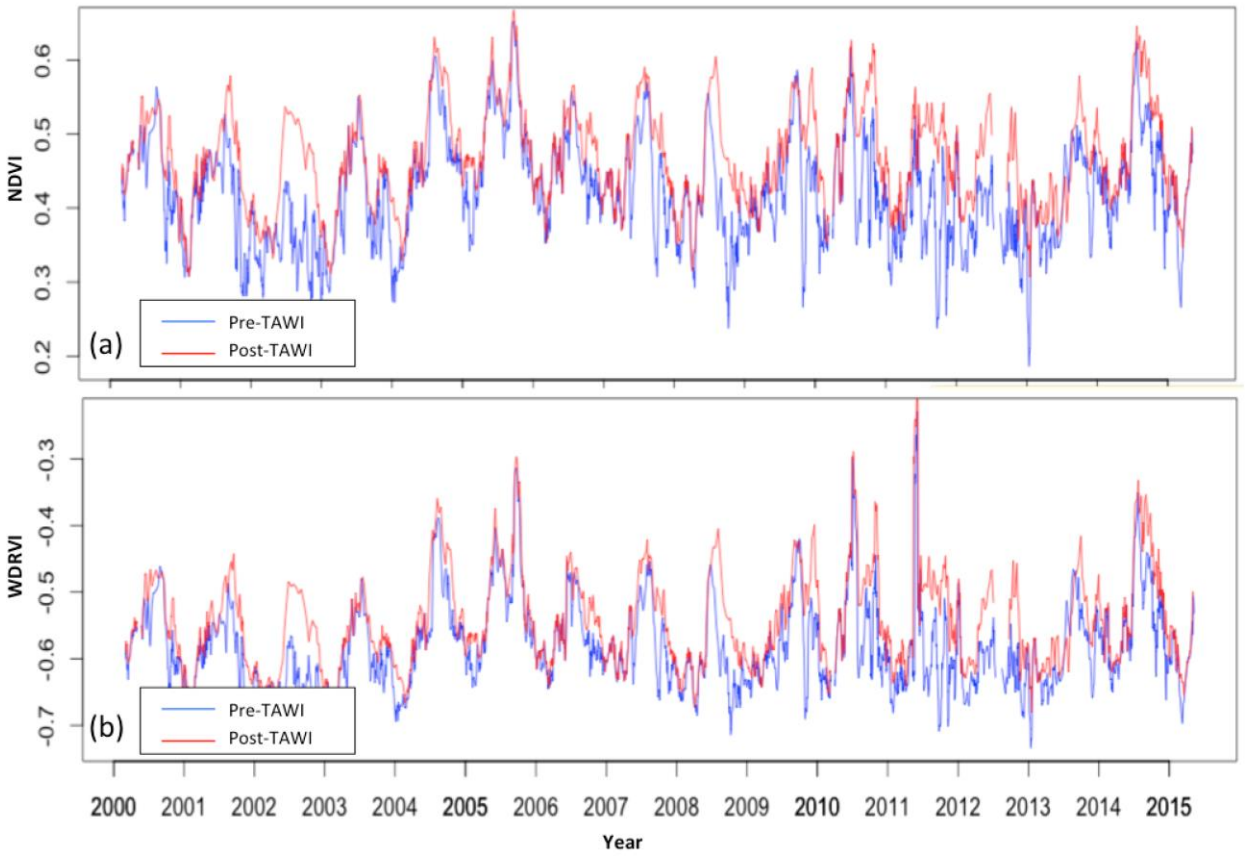


Figure 15. NDVI (a) and WDRVI (b) rolling averages (by eight days) of MODIS cloud-free pixels (pre-TAWI) and non-flooded pixels predicted by the TAWI (post-TAWI) in Pine Harbor, Sapelo River, Georgia, USA.

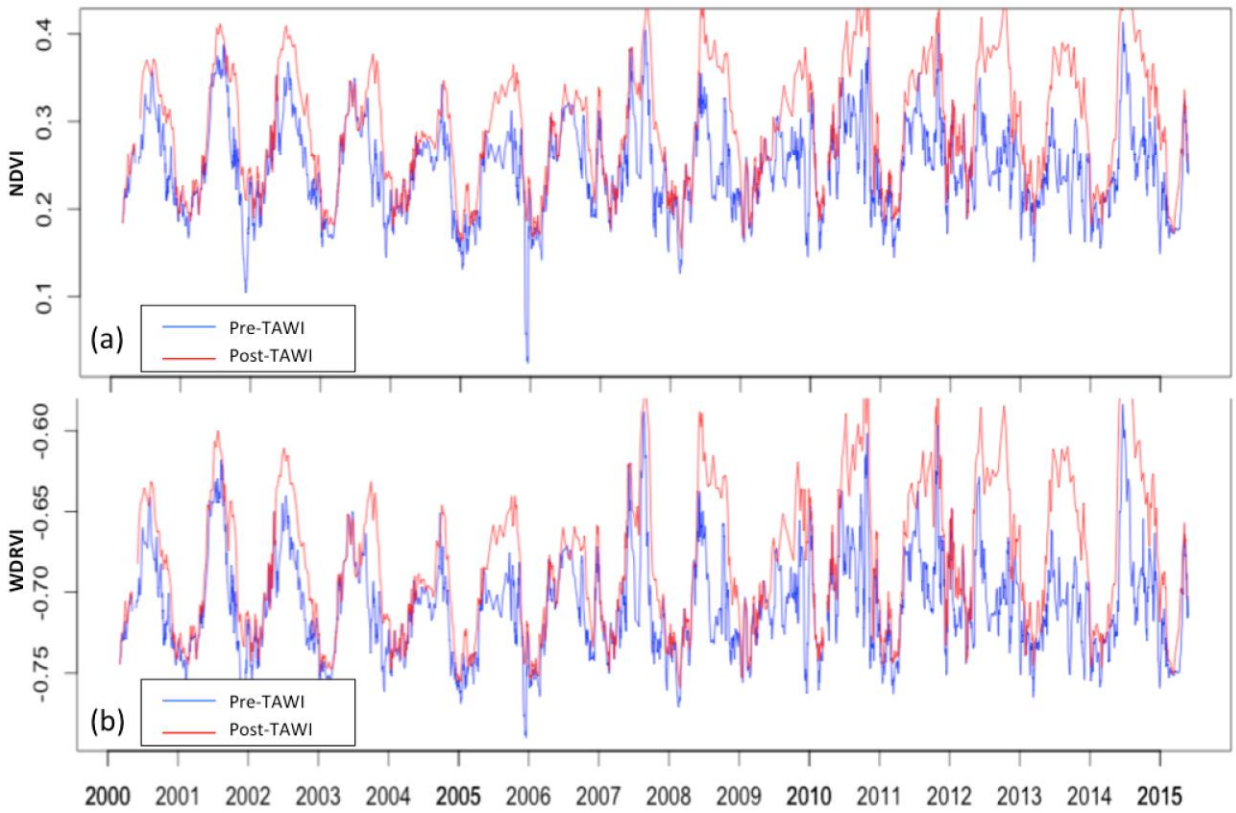


Figure 16. NDVI (a) and WDRVI (b) rolling averages (by eight days) of MODIS cloud-free pixels (pre-TAWI) and non-flooded pixels predicted by the TAWI (post-TAWI) in Garden City Bridge, Main Creek, South Carolina, USA.

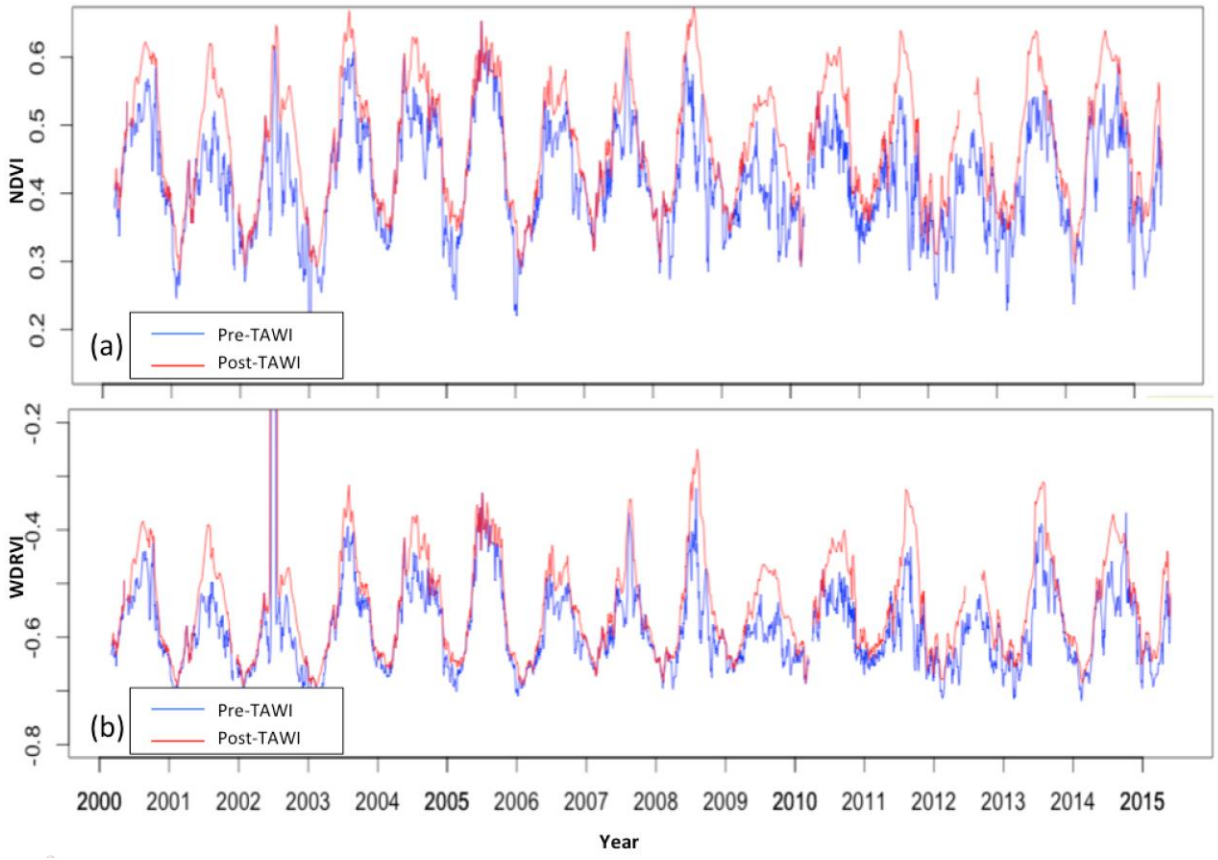


Figure 17. NDVI (a) and WDRVI (b) rolling averages (by eight days) of MODIS cloud-free pixels (pre-TAWI) and non-flooded pixels predicted by the TAWI (post-TAWI) in Southport, North Carolina, USA.

# CHAPTER 4

# DISCUSSIONS

## 4.1 Pre-classification: flagging flooded and non-flooded MODIS pixels

The cloud mask removed 62.8% of MODIS images, leaving 37.2% cloud-free data for analysis across 2000-2015. Cloudy days are common along the Georgia coast due to rain or fog occurrences. Among cloud-free MODIS images from 2013-09-16 to 2015-05-31 (214 images total), 64% were flagged as non-flooded, 15% were flagged as flooded and 21% were unknown flood status. The unknown flood status images accounted for a larger proportion than flooded images, due to the strict rules flagging images, ensuring that the flags were as accurate as possible. Additionally, a mechanical failure caused the PhenoCam to go off line from 2014-07-16 to 2014-09-01 and all images during that time were classified as unknown.

There was no significant difference in average red reflectance of non-flooded and flooded observations in both growing season and non-growing season. The red signals of non-flooded and flooded vegetation are both very weak. However, the average near-infrared reflectance of non-flooded observations was significantly larger than those of flooded observations in both the growing season and non-growing season. Others have found that the near-infrared signal of flooded vegetation is reduced by the water from tide while that of non-flooded vegetation is still strong because of vegetation properties (Lorenzen & Jensen, 1988).

There were some limitations on matching MODIS data and PhenoCam images spatially and temporally. Although the selected two MODIS pixels covered an area of marsh that was both near to the PhenoCam and sampled the majority of the marsh within the PhenoCam field-of

view, these two pixels also covered a small area of forest in the bottom right of pixel 2. As a result, the value of near-infrared reflectance of these two pixels might be higher than that of salt marsh vegetation. Further, the water percentage of the nearest PhenoCam image acquisition that occurred when MODIS passed was used to represent that of the MODIS image, but tidal variation can be great, even within several minutes. Also, there was limitation on defining the flood status of MODIS pixels based on the water percentage values. Visual inspection was used in this step, which requires prior knowledge and expertise. However, a very low cut-off water percentage value (2%) was used to define non-flooded pixels, which would reduce the uncertainty of the flood status of dry marsh. Obvious water appeared in all of the PhenoCam images with water percentage values larger than 6, which would reduce the uncertainty of the flood status of flooded marsh.

### 4.2 Classification: evaluation of logistic regression models and TAWI identifying non-flooded vegetated marsh

The logistic regression model without the phenology predictor explained 21.7% of the variation in flood status of the vegetated marsh. After adding the phenology predictor, the model could explain 29.6% of the variation using either $T_{NDVI}$ or $T_{WDRVI}$ (phenology variables derived from NDVI and WDRVI phenology patterns respectively). Therefore, the logistic regression model was improved by adding predictors that corresponded to change in reflectance over time. The reason is that the reflectance patterns for non-flooded and flooded pixels changed over time. The phenology pattern of non-flooded pixels is because of the vegetation growth and death over time. Although the vegetation in flooded pixels is influenced by water, there is still weak vegetation signal remaining resulting in the phenology patterns of reflectance.

Admittedly, the explained deviance of the improved model was only 29.6%, which demonstrated the model did not fit very well. The deviance is part of because of the heterogeneities of MODIS pixels consists of salt marsh vegetation, forest and creek (see Fig. 5). In addition, most areas of salt marsh are dormant, with little or no aboveground live vegetation remaining during non-growing season (Hammer, 1989). Thus, the spectral signals of vegetation may be too weak to be distinguished from other cover types, which reduced the explained deviance of the model. However, the overall classification accuracy and non-flooded classification accuracy were high, larger than 80% and 95% respectively. In summary, the model could classify the MODIS pixels as flooded and non-flooded accurately although had a relatively low fitness degree.

There were 9 flooded observations misclassified as non-flooded observations, which could reduce the quality of MODIS data of identifying the non-flooded vegetated marsh (Table 7). Several explanations may have contributed to the misclassification. For image a, b and d (Fig. 13), these were flooded non-growing season images. However, these three images had higher NIR reflectance values (larger than 0.12) than those of other flooded observations during the non-growing season (Fig. 18). The logistic regression model suggested that higher NIR reflectance indicates non-flooded vegetation. Thus, perhaps the atmospheric correction produced incorrect NIR surface reflectance values. Alternatively, perhaps algae and other microorganisms in the water lead to a high NIR reflectance for these three observations (Han & Rundquist, 1997). For images c, e and f (Fig. 13), the red and near-infrared reflectance values were consistent with the average red and near-infrared reflectance of corresponding groups (Fig. 11). Thus, it may result from the model classification error. For images g, h and I (Fig. 13), the misclassification may be the true values of these images appear non-flooded. There is mist visible on the lens,

which might have influenced the PhenoCam algorithms to give an incorrect water percentage values for these three images. In summary, the TAWIs performed very well on identifying the non-flooded observations within cloud-free MODIS images since there were only three flooded observations were misclassified as non-flooded due to the model classification error.

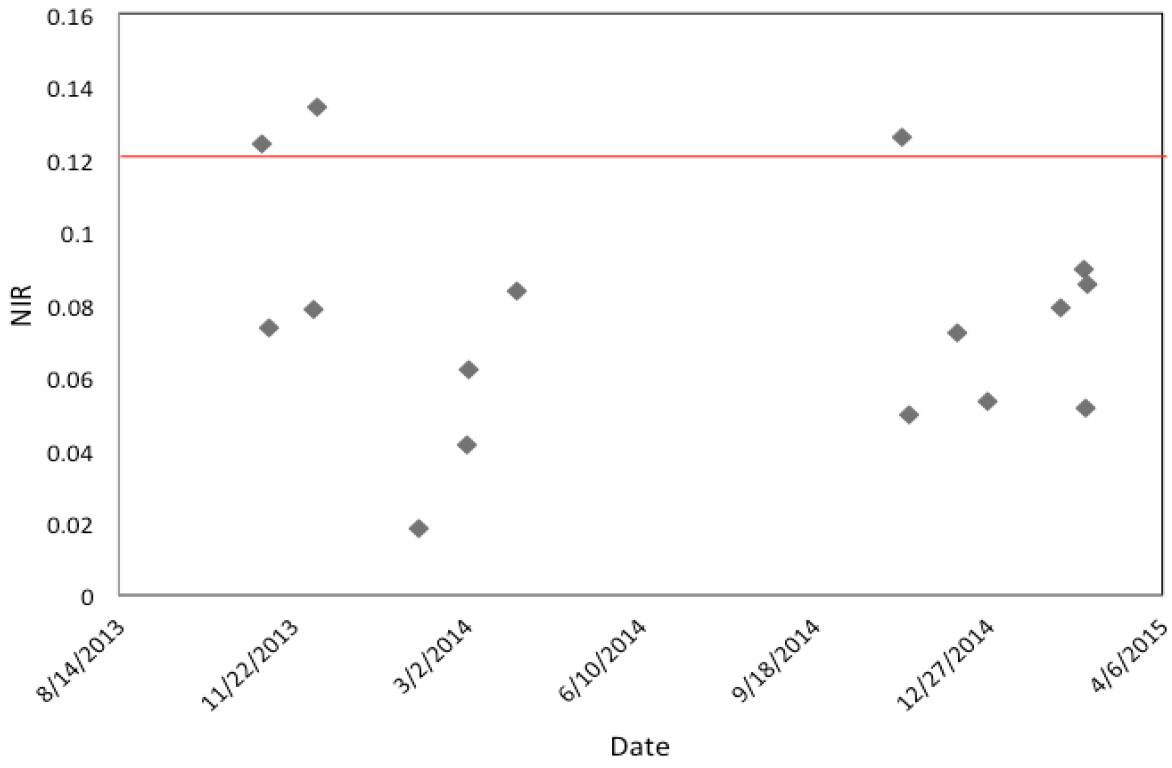


Figure 18. Near-infrared reflectance (NIR) values of flooded observations of non-growing season. The three points above the red line were outliers with high NIR reflectance.

### 4.3 Post-classification: application of tide adjusted wetland index (TAWI) in long time period and different salt marsh sites

Overall phenology derived for 15 years pre- and post-TAWI showed that post-TAWI phenology was able to remove the noise due to tide influence. The phenology patterns were more fluctuated from 2006 than previous years for the three salt marsh sites. Perhaps, the sea level rising leads to more and more flooded days over year (Berry & BenDor, 2015). In addition,

TAWI was applied to three independent sites in Georgia, South Carolina, and North Carolina and produced similar results. The phenology pattern of salt marsh in Georgia was the most fluctuated, followed by South Carolina, and then North Carolina. TAWI worked best in areas where tide influence was the worst (Georgia). However, there was restriction on applying TAWI to salt marsh sites in different places. TAWI is calculated by red, NIR reflectance and phenology patterns variable. The phenology patterns changed over different places, such as peak day, growing season and non-growing season. Thus, the TAWI derived from Georgia phenology only can be used in the places where the phenology is similar to Georgia, such as South Carolina and North Carolina. In the future, the phenology-adjusted parameters will be added to TAWI equations to increase the applicability of TAWI in the salt marshes which have different phenology patterns to Georgia, such as Louisiana.

# CHAPTER 5

# CONCLUSIONS

This research presented a novel index, TAWI (tide adjusted wetland index) for identifying and eliminating tide affected salt marsh images from temporally dense and spatially coarse MODIS data. TAWI can be used to filter out flooded vegetation from MODIS daily products to avoid daily variability within salt marsh biophysical parameters due to tidal fluctuations. Incorporating the phenology variable to the logistic regression model improved the classification results, explaining the variation of vegetated marsh better. Overall phenology derived for 15 years pre- and post-TAWI showed that post-TAWI phenology was able to remove the noise due to tide influence. TAWI was applied to multiple independent salt marsh sites in Georgia, South Carolina and North Carolina and produced similar results. TAWI works best in areas where tide influence is the worst (such as Georgia). Eliminating flooded data from salt marsh phenology using TAWI will provide accurate remote estimation for numerous biophysical parameters including chlorophyll content, above and below ground biomass, and gross primary productivity which are the proxy for salt marsh health and productivity.

One of the challenges of this study was to spatially match PhenoCam images with relatively low spatial resolution MODIS data (250m). There are upcoming satellite missions those would be highly suitable for furthering the analysis presented in this study. For example, Sentinel-2, the European wide-swath, high-resolution, multi-spectral imaging mission with a spatial resolution of 10m in visible and short-wave infrared bands, which may produce higher explained deviance than MODIS data (Drusch, 2012). However, Sentinel-2 provides a revisit

time of 5 days at the equator in cloud-free conditions (Drusch, 2012), which may not suit the tide variation well. In addition, the logistic regression model based on red and near-infrared reflectance may not explain all the variations of salt marsh vegetation. In the future, more bands should be included to develop the logistic regression classification model, such as blue, thermal band or other narrow bands. Therefore, NASA's upcoming hyperspectral sensor such as Hyperspectral Infrared Imager (HyspIRI) and GEOstationary Coastal and Air Pollution Events (GEO-CAPE) data should also be useful and may improve the classification result.

REFERENCES

Adam, E., Mutanga, O., & Rugege, D. (2010). Multispectral and hyperspectral remote sensing for identification and mapping of wetland vegetation: a review. Wetlands Ecology and Management, 18(3), 281-296.

Alongi, D. M. (1998). Coastal Ecosystem Processes (Vol. 15). CRC press.

Artigas, F., & Pechmann, I. C. (2010). Balloon imagery verification of remotely sensed Phragmites australis expansion in an urban estuary of New Jersey, USA. Landscape and Urban Planning, 95, 105-112.

Atkinson, P.M. and Massari, R., 1998, Generalized linear modeling of susceptibility to landsliding in the central Apennines, Italy. Computer and Geosciences,24, pp. 373–385.

Barr, J. (2013). Modeling Light Use Efficiency in a Subtropical Mangrove Forest Equipped with CO2 Eddy Covariance °C. FCE LTER Journal Articles.

Berry, M., & BenDor, T. K. (2015). Integrating sea level rise into development suitability analysis. Computers, Environment and Urban Systems, 51, 13–24.

Braak, C. J. F. T., & Tongeren, O. F. R. van. (1995). Data Analysis in Community and Landscape Ecology. Cambridge University Press.

Bryant, J. C., & Chabreck, R. H. (1998). Effects of impoundment on vertical accretion coastal marsh. Estuaries, 21, 416-422.

Butera, M. K. (1983). Remote sensing of wetlands. Geoscience and Remote Sensing, IEEE Transactions on, (3), 383-392.

Chmura, G. L., Anisfeld, S. C., Cahoon, D. R., & Lynch, J. C. (2003). Global carbon sequestration in tidal, saline wetland soils. Global Biogeochemical Cycles, 17, 1111.

Collin, A., Long, B., & Archambault, P. (2010). Salt-marsh characterization, zonation assessment and mapping through a dual-wavelength LiDAR. Remote Sensing of Environment, 114, 520-530.

Connor, R. F., Chmura, G. L., & Beecher, C. B. (2001). Carbon accumulation in Bay of Fundy salt marshes: Implications for restoration of reclaimed marshes. Global Biogeochemical Cycles, 15, 943-954.

Davranche, A., Lefebvre, G., & Poulin, B. (2010). Wetland monitoring using classification trees and SPOT-5 seasonal time series. Remote sensing of Environment, 114, 552-562.

DeFries, R. S., & Townshend, J. R. G. (1994). NDVI-derived land cover classifications at a global scale. International Journal of Remote Sensing, 15(17), 3567-3586.

Drusch, M., Del Bello, U., Carlier, S., Colin, O., Fernandez, V., Gascon, F., ... & Bargellini, P. (2012). Sentinel-2: ESA's optical high-resolution mission for GMES operational services. *Remote Sensing of Environment*, *120*, 25-36.

Duncan, H. W., & Duncan, B. M. (1987). The Smithsonian guide to seaside plants of the Gulf and Atlantic Coasts from Louisiana to Massachusetts, exclusive of lower peninsular Florida. Washington, DC: Smithsonian Institution Press, 409.

Efron, B. (1983). Estimating the error rate of a prediction rule: improvement on cross-validation. Journal of the American Statistical Association, 78(382), 316-331.

Eisma, D. A., Eisma, D., & Oer, P. D. B. (1998). Intertidal deposits: river mouths, tidal flats, and coastal lagoons (Vol. 16). CRC press.

Freedman, D. A. (2009). Statistical Models: Theory and Practice. Cambridge University Press.

Gallagher, J. L., Reimold, R. J., Linthurst, R. A., & Pfeiffer, W. J. (1980). Aerial production, mortality, and mineral accumulation-export dynamics in Spartina alterniflora and Juncus roemerianus plant stands in a Georgia salt marsh. Ecology, 6, 303-312.

Gilfillan, E. S., Page, D. S., Bass, A. E., Foster, J. C., Fickett, P. M., Ellis, W. G. H., Rusk, S., & Brown, C. (1989). Use of Na/K ratios in leaf tissues to determine effects of petroleum on salt exclusion in marine halophytes. Marine Pollution Bulletin, 20, 272-276.

Gitelson, A. A. (2004). Wide Dynamic Range Vegetation Index for remote quantification of biophysical characteristics of vegetation. Journal of Plant Physiology, 161(2), 165–173.

Gross, M. F., & Klemas, V. (1986). The use of airborne imaging spectrometer (AIS) data to differentiate marsh vegetation. Remote Sensing of Environment, 19, 97-103.

Hackney, C. T., & Yelverton, G. F. (1990). Effects of human activities and sea level rise on wetland ecosystems in the Cape Fear River Estuary, North Carolina, USA. Wetland Ecology and Management: Case Studies Tasks for Vegetation Science, 25, 55-61.

Hammer, D. A. (1989). Constructed Wetlands for Wastewater Treatment: Municipal, Industrial and Agricultural. CRC Press.

Han, L., & Rundquist, D. C. (1997). Comparison of NIR/RED ratio and first derivative of reflectance in estimating algal-chlorophyll concentration: A case study in a turbid reservoir. Remote Sensing of Environment, 62(3), 253–261.

Harbor, J.M. (2007). A practical method for estimating the impact of land-use change on surface runoff, groundwater recharge and wetland hydrology. Journal of the American Planning Association, 60, 95-108.

Hastie, T. J. and Pregibon, D. (1992) Generalized linear models. Chapter 6 of Statistical Models in S eds J. M. Chambers and T. J. Hastie, Wadsworth & Brooks/Cole.

Hardisky, M. A., Daiber, F. C., Roman, C. T., & Klemas, V. (1984). Remote sensing of biomass and annual net aerial primary productivity of a salt marsh. Remote Sensing of Environment, 16(2), 91-106.

Hester, M. W., & Mendelssohn, I. A. (2000). Long-term recovery of a Louisiana brackish marsh plant community from oil-spill impact; vegetation response and mitigating effects of marsh surface elevation. Marine Environmental Research, 49, 233-254.

Holbert. K. E. (2007). Solar Energy Calulations. Handbook of renewable energy technology. Charpter 8, pp 193.

Howland WG (1980) Multispectral aerial photography for wetland vegetation mapping. Photogramm Eng Remote Sensing 46:87–99

Jensen, J. R., & Lulla, D. K. (1987). Introductory digital image processing: A remote sensing perspective. Geocarto International, 2(1), 65–65.

Kaufman, L., & Rousseeuw, P. J. (2009). Clustering Large Applications (Program CLARA). In Finding Groups in Data: An Introduction to Cluster Analysis (pp. 126–163). Hoboken, NJ, USA: John Wiley & Sons.

Klemas, V. (2011). Remote sensing of wetlands: case studies comparing practical techniques. Journal of Coastal Research, 27(3), 418-427.

Kohavi, R. (1995). A study of cross-validation and bootstrap for accuracy estimation and model selection. In Ijcai, 14(2), 1137-1145

Kurths, J., & Herzel, H. (1987). An attractor in a solar time series. Physica D: Nonlinear Phenomena, 25(1–3), 165–172

Lorenzen, B., & Jensen, A. (1988). Reflectance of blue, green, red and near infrared radiation from wetland vegetation used in a model discriminating live and dead above ground biomass. New Phytologist, 108(3), 345–355.

Malthus, T. J., & George, D. G. (1997). Airborne remote sensing of marcrophytes in Cefni Reservoir, Anglesey, UK. Aquatic Botany, 58, 317-332.

Matthiopoulos J. (2013). How to be a Quantitative Ecologist: The 'A to R' of Green Mathematics and Statistics. International Statistical Review, 81(1), 158.

Mishra, D. R., & Ghosh, S. (2013). Moderate resolution satellite data for mapping salt marshes. SPIE Newsroom.

Mishra, D. R., & Ghosh, S. (2015). Using Moderate-Resolution Satellite Sensors for Monitoring the Biophysical Parameters and Phenology of Tidal Marshes. Remote Sensing of Wetlands: Applications and Advances, 283.

Mishra, D. R., Cho, H. J., Ghosh, S., Fox, A., Downs, C., Merani, P. B. T., Kirui, P., Jackson, N. & Mishra, S. (2012). Post-spill state of the salt marsh: Remote estimation of the ecological impact of the Gulf of Mexico oil spill on Louisiana Salt Marshes. Remote Sensing of Environment, 118, 176-185.

Mitsch, W. J., & Gosselink, J. G. (2007). Wetlands. John Wiley and Sons.

Neteler, M. (2005). Time series processing of MODIS satellite data for landscape epidemiological applications. International Journal of Geoinformatics, 1, 133-138.

Odum, W.E. 1998. Comparative ecology of tidal freshwater and salt marshes. Annual Review of Ecology and Systematics 19: 147–176.

Odum, W.E., T.J. Smith, J.K. Hoover, and C.C. McIvor. 1984. The ecology of tidal freshwater marshes of the United States East Coast: A community profile. Washington, DC: U.S. Fish and Wildlife Service Report FWS/OBS-83/17.

Ozesmi, S. L., & Bauer, M. E. (2002). Satellite remote sensing of wetlands. Wetlands ecology and management, 10(5), 381-402.

Papale, D., Reichstein, M., Aubinet, M., Canfora, E., Bernhofer, C., Kutsch, W., … Yakir, D. (2006). Towards a standardized processing of Net Ecosystem Exchange measured with eddy covariance technique: algorithms and uncertainty estimation. Biogeosciences, 3(4), 571–583.

Ravens, T. M., Thomos, R. C., Roberts, K. A., & Santschi, P. H. (2009). Causes of salt marsh erosion in Galveston Bay, Texas. Journal of Coastal Research, 25, 265-272.

Rebelo, L. M., Finlayson, C. M., & Nagabhatla, N. (2009). Remote sensing and GIS for wetland inventory, mapping and change analysis. Journal of environmental management, 90(7), 2144-2153.

Richardson, A. D., Jenkins, J. P., Braswell, B. H., Hollinger, D. Y., Ollinger, S. V., & Smith, M.-L. (2007). Use of digital webcam images to track spring green-up in a deciduous broadleaf forest. Oecologia, 152(2), 323–334.

Richardson, A. D., Friedl, M. A., Frolking, S., & Pless, R., PhenoCam Collaborators. (2011). PhenoCam: A continental-scale observatory for monitoring the phenology of terrestrial vegetation. AGU Fall Meeting Abstracts, 11, 0517.

Rundquist, D. C., Narumalani, S., & Narayanan, R. M. (2001). A review of wetlands remote sensing and defining new considerations.

Seher, J. S., & Tueller, P. T. (1973). Color aerial photos for marshland. Photogrammetric Engineering, 9(5).

Shima LJ, Anderson RR, Carter VP et al (1976) The use of aerial color infrared photography in mapping the vegeta- tion of freshwater marsh. Chesap Sci 17:74–85

Silliman, B. R., Grosholz, E. D., & Bertness, M. D. (Eds). (2009). Human impacts on Salt Marshes: A Global Perspective. University of California Press.

Smith, C. J., DeLaune, R. D., & Patrick, Jr. (1983). Carbon dioxide emission and carbon accumulation in coastal wetlands. Estuarine, Coastal and Shelf Science, 17: 21-29.

Sugumaran, R., Meyer, J. C., & Davis, J. (2004). A web-based environmental decision support system (WEDSS) for environmental planning and watershed management. Journal of Geographical Systems, 6, 307-322.

Swenson, E. M., & Turner, R. E. (1987). Spoil banks: Effects on a coastal marsh water-level regime. Estuaries, Coastal and Shelf Science, 24, 599-609.

Vermote, E. F., Kotchenova, S. Y., & Ray, J. P. (2011). MODIS surface reflectance user's guide. MODIS Land Surface Reflectance Science Computing Facility, version, 1.

Walker, S. H., & Duncan, D. B. (1967). Estimation of the probability of an event as a function of several independent variables. *Biometrika* **54**: 167–178.

White, W. A., & Morton, R. A. (1997). Wetland losses related to fault movement and hydrocarbon production, southern Texas coast. Journal of Coastal Research, 13, 1305-1320.

Więski, K., & Pennings, S. C. (2013). Climate Drivers of Spartina alterniflora Saltmarsh Production in Georgia, USA. Ecosystems, 17(3), 473–484.

Zuur, A., Ieno, E., Walker, N., Saveliev, A., & Smith, G. (2009). Mixedeffects models and extensions in ecology with R. New York, NY, USA: Springer.